Seismo-tectonics around Lhasa, Tibet

Master Thesis

By

Laba Ciren

Institute of Earth Science University of Bergen, Norway

May 2011

Acknowledgement

Bergen, May 2011

Laba Ciren

Table of Contents

Chapter 1

Introduction

An earthquake with its sudden, unprepared and usually tragic destruction is considered one of the most terrible natural disasters that threaten human survival and development. Tibet is the main part of the Qinghai-Tibet Plateau, located in the Mediterranean-South Asia earthquake zone, which is one of the main seismic zones of the Earth. Therefore, Tibet and its surroundings is one of the most active regions in terms of tectonics and seismicity in the world. Usually seismicity is characterized by earthquakes with maximum magnitude of about 6.5 (Ni and York, 1978). According to Technology and Archives (1982), there were 562 earthquakes with magnitudes ranging from 4.7 to 8.5 in this region between 1900 and 1982. Based on the Incorporated Research Institutions for Seismology (IRIS) and Global Centroid Moment Tensor (GCMT) catalogue, approximately 54 earthquakes with moment magnitudes greater than 5.0 occurred in the Tibetan Plateau within the period 1990 to 2010 (Table 2.1). In addition, three large earthquakes with magnitude 8.0 took place in the Tibetan Plateau in 1411, 1806 and 1833 (Technology and Archives, 1982).

A brief background of the Tibetan Plateau tectonics and the seismic station in Tibet is given in chapter 2. Landsat image interpretation and the fault plane solutions of earthquakes suggest that normal faulting characterizes the present tectonics of the Tibetan Plateau (Molnar and Tapponnier, 1978; Ni and York, 1978). I will also use fault plane solutions of 54 earthquakes with magnitudes ranging from 5.0 to 7.8, collected from the global CMT catalogue, on the Tibetan Plateau between 1990 and 2010 to further study the character of faulting in the Tibetan Plateau in this section.

The Mw6.3 Damxung earthquake of 6 October, 2008 occurred at the village of Yangyi, in the south of Damxung county, with a death toll of 10 people and the collapse of 147 houses (Gao *et al.*, 2010; Qiao *et al.*, 2010; Qiao *et al.*, 2009; Wu *et al.*, 2010) (http://baike.baidu. com/view/2406293). Between 1925 and 1972, about 25 earthquakes with magnitudes greater than 4.7 occurred in this area, including the two large earthquakes with magnitudes 8.0 and 7.5 in 1951 and 1952. Moreover, an earthquake

(M=8.0) happened in this region in 1411. The background of the 6 October, 2008 Damxung earthquake and surrounding tectonics will be explained in chapter 3.

On 30 July 1992, an earthquake of magnitude Mw6.1 occurred in the Nyimo county (29°35′N, 90°15′E), situated at the northwestern end of the Damxung-Yangbajain rift, west of Lhasa. The location of the earthquake was close to the epicenter of the 2008 Damxung earthquake; both earthquakes occurred in the same active tectonic belt (http://www.cqvip.com/qk/88497x/200902/30824658.html).

We know that when an earthquake occurs most of the energy is propagated in the form of seismic waves, and the body-wave recorded data is important in order to study the focal mechanism and the dynamic rupture process of the fault. Generally, in order to obtain more precise focal mechanisms and source rupture processes, it is necessary to record data in the near-field moderate or strong ground-motion with high time-space-resolution etc. Due to the conditional constraints at the Tibetan Plateau, these near-field observations are usually lacking.

The seismic moment tensor inversion method is widely employed in determining the focal mechanism and the kinematic rupture process of a fault. The inversion study of the rupture process began in the early 1980s. After several years of development, gradually a variety of the different inversion methods has been formed, e.g. the body wave inversion method (Barker and Langston, 1981; Barker and Langston, 1983; Estabrook, 1999; Kikuchi and Kanamori, 1982; Kikuchi and Kanamori, 1986; Kikuchi and Kanamori, 1991; Shomali and Slunga, 2000).

In chapter 4, I will use the teleseismic body-wave inversion methodology by Kikuchi and Kanamori (1982; 1986; 1991) with their program (2003) to determine the focal mechanism, source depth and seismic moment for the 2008 Damxung and 1992 Nyimo earthquakes. The broadband teleseismic seismograms for this inversion are collected from the Global Seismographic Network (GSN) stations at teleseismic distances (30° < Δ < 90°). I am also interested in comparing the results of the focal mechanisms of two events to further understand the properties of earthquakes in this region.

The stochastic simulation modeling technique is an important tool for predicting ground motions near the rupture of large earthquakes. The point-source stochastic simulation method (Boore, 1983; Boore, 1996; Boore and Atkinson, 1987; Hanks and

Mcguire, 1981; Ou and Herrmann, 1990) has been extended to a finite-fault source stochastic simulation method based on a static corner frequency (Beresnev and Atkinson, 1997; Beresnev and Atkinson, 1998a; Beresnev and Atkinson, 1998b; Castro and Ruı́z-Cruz, 2005; Ghasemi *et al.*, 2010; Roumelioti and Beresnev, 2003; Shoja-Taheri and Ghofrani, 2007). It has been further improved based on a dynamic corner frequency by Motazedian and Atkinson (2005), and Motazedian and Moinfar (2006). In this model, a large finite-fault is divided into a number of small rectangular subfaults, where each one is considered as a point source, and the center of the subfault is assumed as the location of the point source. The rupture starts at the hypocenter and propagates radially from it.

In chapter 5, I will use the stochastic finite-fault methodology based on dynamic corner frequency with the algorithm EXSIM (Motazedian, 2009) to predict the ground motion at the LSA station for the 2008 Damxung earthquake. Some parameters of the simulation will be adopted from my previous results of moment tensor inversion. The ground-motion data used for comparison is collected from the Global Seismographic Network broadband stations of IRIS-DMC. The purpose of this chapter is to calibrate the source parameters of the Damxung earthquake, such as anelastic attenuation, geometrical spreading and stress drop.

The conclusion and discussion will be presented in chapter 6 and chapter 7 respectively.

Chapter 2

Tectonics of the Tibetan Plateau

2.1 Geological background of the Tibetan Plateau

The Tibetan Plateau stretches from 26°00′12″N-39°46′50″N, and from 73°18′52″E - 104°46′59″E, covering an area of approximately 2572400 sq km (Pan, 1999; Xing *et al.*, 2007; Zhang *et al.*, 2002). Referred to by Tibetans as the "Roof of the World" it is the Earth's largest and highest plateau, with an average elevation of about 5 km (Ni and York, 1978; Pan, 1999). It is surrounded to the south and west by the Himalayan and Karakorum ranges and to the north by the Kunlun and Altyn Tagh mountain regions. Its eastern boundary is given by the Hengduan Mountains, which consist of several parallel mountain ranges on the border between western Yunnan and Sichuan and east Tibet (Figure 2.1).
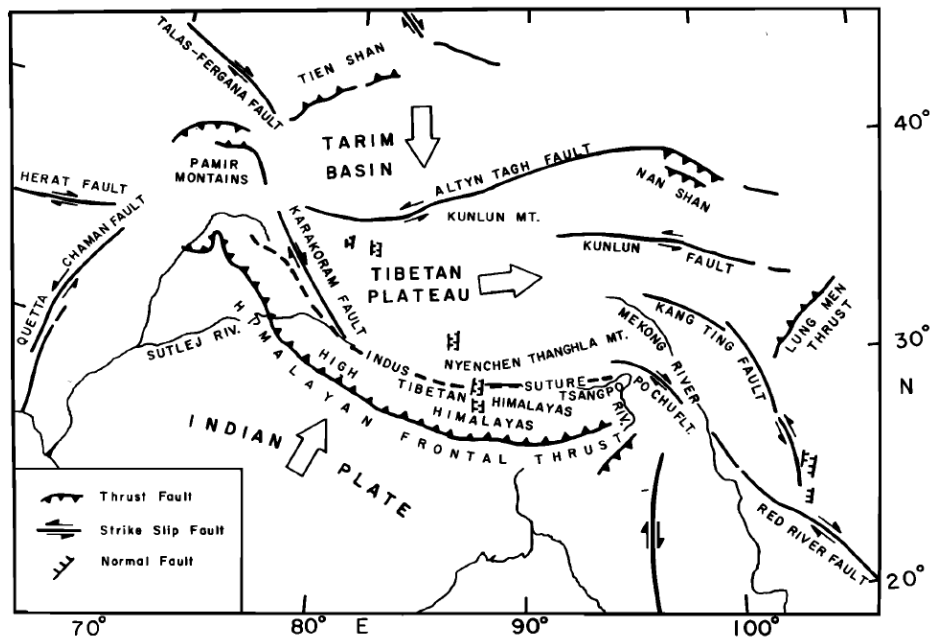

Figure 2.1 Simplified map of geography and tectonics in the Tibetan Plateau. From (Ni and York, 1978)

The Indian and Eurasian plates interaction resulted in the Himalayas and the Tibetan Plateau uplift, and caused strong tectonic movement within the plateau. The Tibetan Plateau is seismically moderately active (Fielding *et al.*, 1994; Mercier *et al.*, 1987; Molnar and Tapponnier, 1978; Ni and York, 1978; Xing *et al*., 2007).

2.2 Active tectonic characteristics of the fault block regions

The Tibetan Plateau was built on a complex tectonic collage that is separated into a number of blocks by sutures (Figure 2.2). From south to north the blocks are the Himalaya block (HB), Lhasa block (LB), Qiangtang block (QB), Bayan Har block (BHB) and Qaidam block (QB). The HB was the northern marine margin of the Indian continent (Mercier *et al.*, 1987) and the MCT (Main Central Thrust) fault zone as well as the MBT (Main Boundary Thrust) zone (Deng *et al*., 2003; Zeng *et al*., 2000). The LB is bound by the Indus-Tsangpo suture (IST) and Banggong-Nujiang suture (NBS), extending W–E for several hundred km (Hou *et al.*, 2009). It represented the southern border of Asia during the Cretaceous-Eocene times (Mercier *et al.*, 1987) and consists of 7 approximately N-S trending norm fault and graben systems (Armijo *et al.*, 1986; Deng *et al*., 2003; Zeng *et al*., 2000). The QB dominantly consists of metamorphic rocks and late Paleozoic shallow marine strata and Jurassic–Cretaceous marine carbonate rocks interbedded with terrestrial clastic rocks (Hou *et al*., 2009), bounded by NBS and JSS (Jinsha suture).

The Tibetan Plateau has a thick crust, while the lithosphere is relatively thin. Thus, the crust of the plateau is approximately twice the thickness of the normal continental crust (Dewey *et al.*, 1988; Li, 2004; Li *et al.*, 2010; Mercier *et al*., 1987; Pan, 1999; Rthery and Drury, 1984; Zhang *et al.*, 2007). However, on the Tibetan Plateau the crustal thickness varies from block to block.
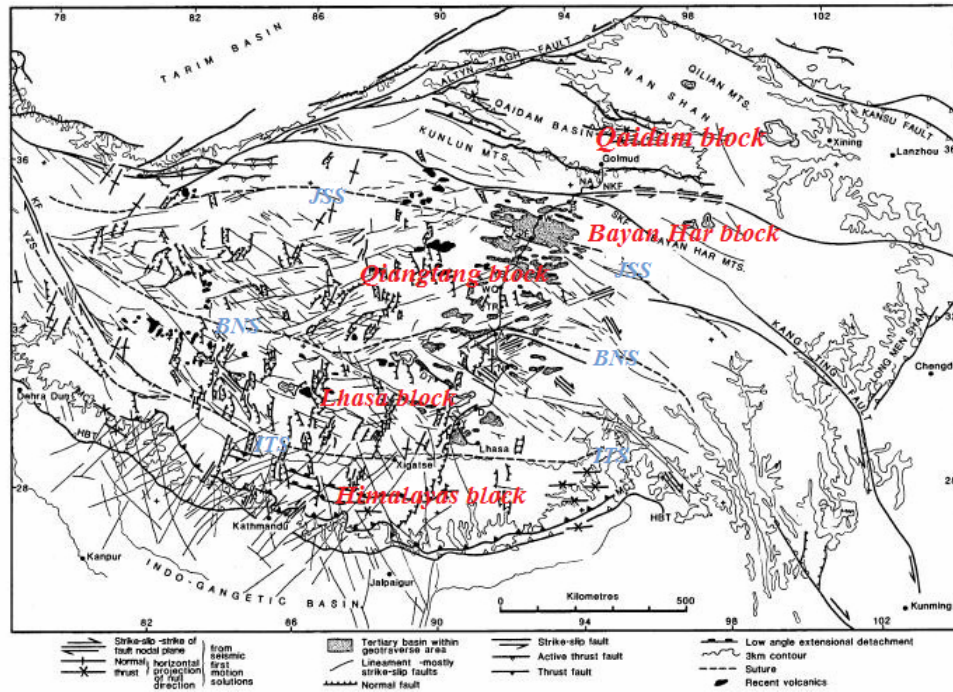
Figure 2.2 *Tectonic map of the Qinghai-Tibet plateau. ITS: Indus-Tsangpo suture,* BNS*: Banggong-Nujiang suture,* JSS: *Jinsha suture. Modified from (Dewey et al., 1988)*

Based on Zhang *et al.* (2008), beneath the Himalayan block, the crustal thickness is about 60 km; the lithosphere thickness is about 155 km and the asthenosphere gradually thickens from south to north. Beneath the Lhasa block, the crustal thickness is approximately between 60 and 70 km; the lithosphere thickness approximately 160 km. Beneath the Qiangtang block, the thickness of the crust and lithosphere are about 75 km and 130 km respectively, and the asthenosphere is very thick. Beneath the Bayan Har block, the crustal thickness thins to about 65 km, while the lithosphere gradually thickens to 150~160 km. The thickness of the asthenosphere, however, is decreasing (Figure 2.3).

There are probably 1-2 lower velocity and higher conductivity zones beneath the Tibetan Plateau (Dewey *et al.*, 1988; Pan, 1999). This reveals the complexity of the plateau's crustal structure, with a multilayered structure of alternately soft and hard rock layers. In the Tibetan Plateau, the shear wave velocity is basically a gradient and at the depth of Moho an average velocity reaches about 3.5 km/s.
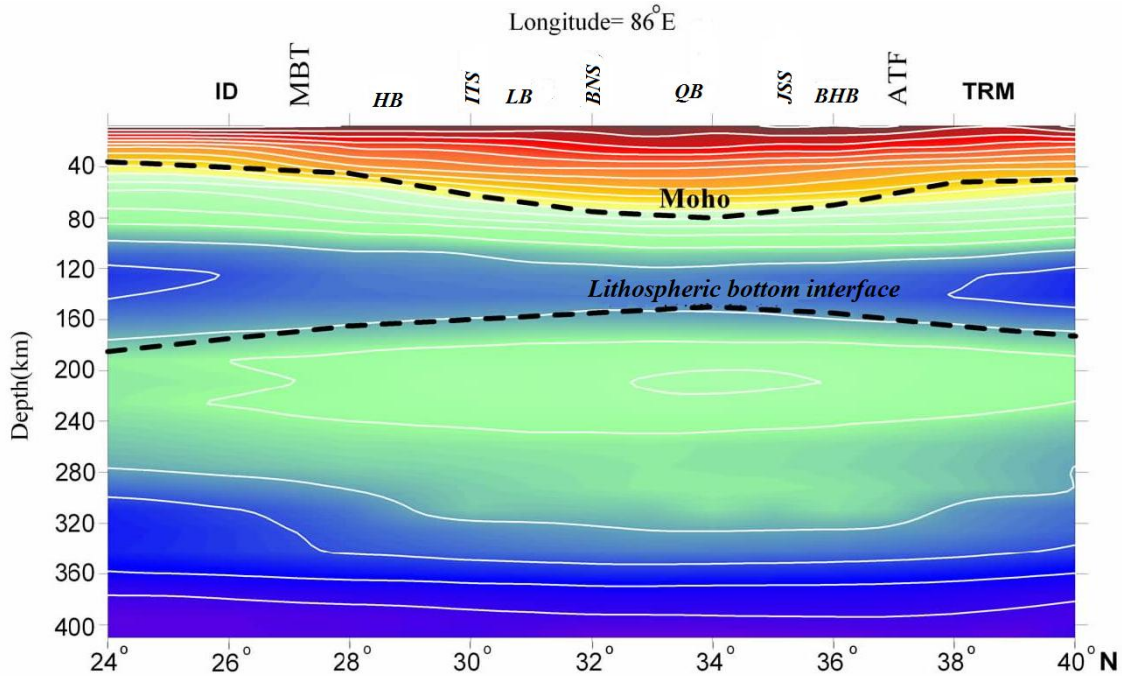
Figure 2.3 *The crustal and lithospheric thickness along the profile* 86º *E. From (Zhang et al., 2008).*

2.3 Fault plane solutions

The fault plane solutions (Figure 2.4) within the Tibetan Plateau and its surroundings between 1900 and 1988 by Molnar *et al.* (1993) imply that the central portion of the Plateau is dominated by normal faulting and horizontal extension, while the thrust faulting and horizontal compression characterize deformation on its border.

Furthermore, the fault plane solutions of the 54 earthquakes on the Tibetan Plateau in the period of 1990 to 2010 from GCMT catalogue are plotted in Figure 2.5. The data set includes 30 normal slip faulting, 11strike slip faulting and 12 thrust slip faulting with focal depths of all of these earthquakes between 10 and 30 km.

The fault plane solutions (Figure 2.5) show that the normal faulting and strike slip predominate within the high part of the Tibetan Plateau, located within latitude range of about 29º - 36º N and longitude range of 80º - 96º N. For example, the solutions of earthquakes number 7, 4 and 23 (Figure 2.5) are strike slip and they were just located

near the Beng Co fault, which is a right lateral strike-slip fault zone that was activated by the magnitude 8 and 7.5 earthquakes of 1951 and 1952 (Tapponnier *et al.*, 1981). The solutions of earthquakes number 1, 2, 3, 35 and 26 (Figure 2.5) are normal faulting, and they are situated along the Yadong-Gulu rift, which is the longest rift system of Tibet and normal fault zone (Armijo *et al.*, 1986; Chen *et al.*, 2004; Cogan *et al.*, 1998; Mercier *et al.*, 987; Ni and Barazang, 1984; Wu *et al.,* 2010; Zhao *et al.*, 2001). A large earthquake with magnitude 8.0 occurred in this region in 1411 (Technology and Archives, 1982; Wu *et al.*, 1990). Most of the solutions have approximately east-west trending T axes and the normal slip faulting roughly strikes in north-south direction. The type of faulting in Table 2.1 was assigned through my interpretation of the plotted solution.
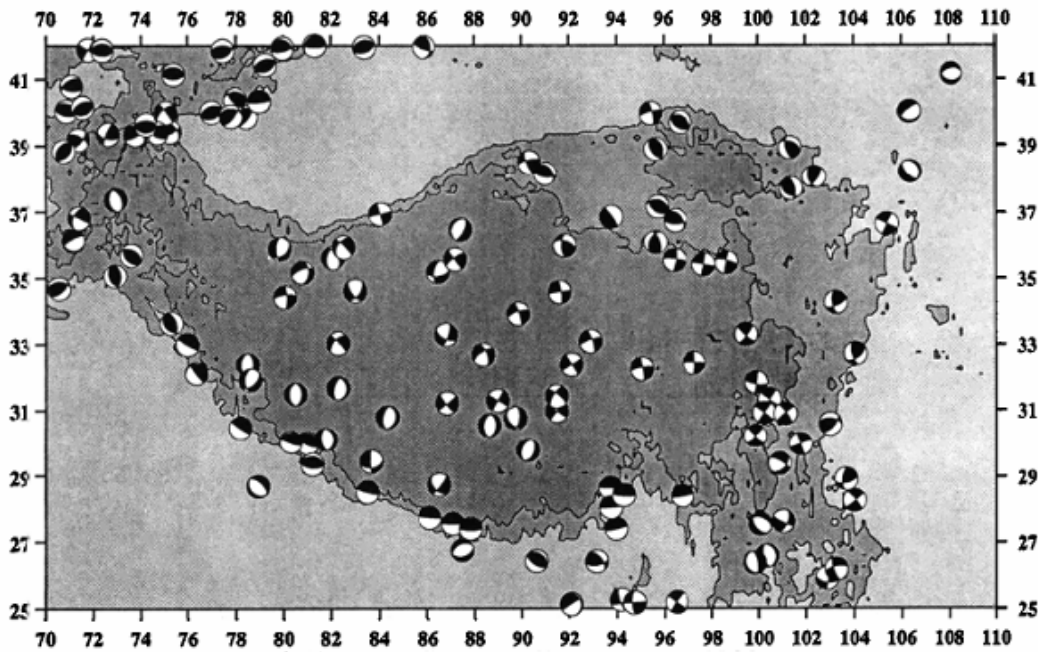
Figure 2.4 Map of the Tibetan Plateau showing lower hemisphere projections of fault plane solutions of earthquakes within Tibet and its surroundings between 1900 and 1988. From Molnar et al. (1993).
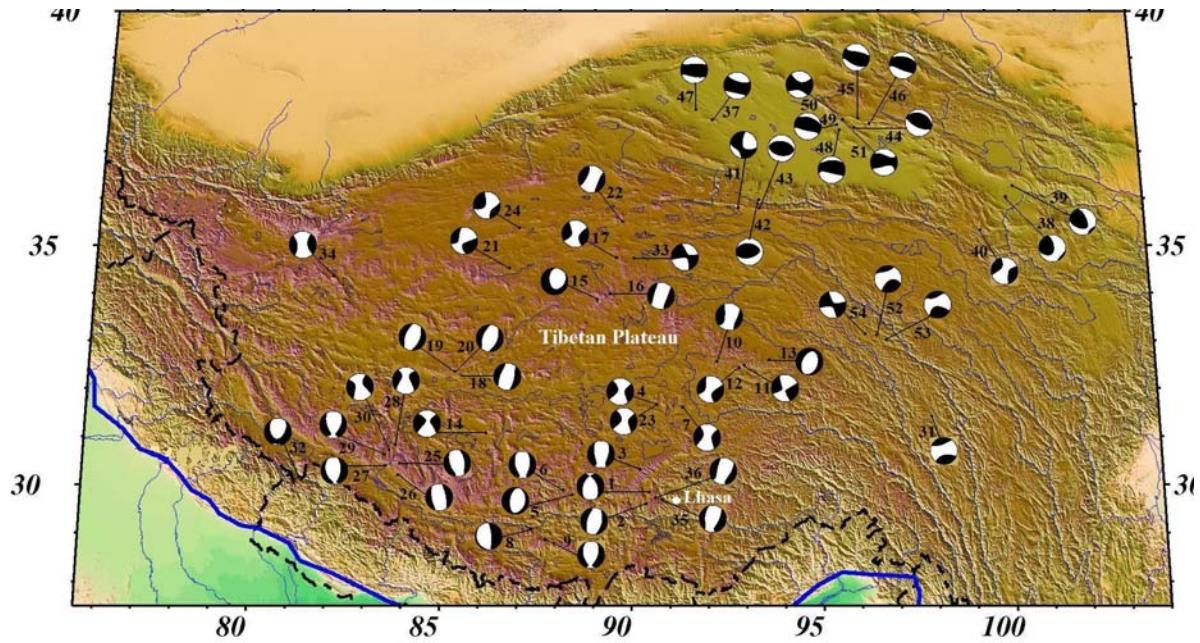
Figure 2.5 *Fault plane solutions of earthquakes within the Qinghai-Tibet Plateau between 1990 and 2010. The focal mechanism solutions were collected from the global CMT catalogue. The fault plane solutions numbered 1-54 correspond to earthquakes listed in Table 2.1. Solid circle are locations of earthquake epicenters.*

Table 2.1 Earthquake (Mw≥5.0) with fault plane solutions within Tibetan Plateau between 1990 and 2010

No.	Date y-m-d	Lat. (ºN)	Long. (ºE)	Mag. (M_w)	Depth (km)	Type of Mechanism
1	2010.11.30	29.78	90.51	5.3	19.0	Normal
2	1992.07.30	29.46	90.30	6.1	15.0	Normal
3	1993.01.18	30.34	90.28	5.9	15.0	Normal
4	2006.04.19	31.61	90.67	5.7	23.2	Strike-slip
5	1998.07.20	29.83	88.47	5.7	15.0	Normal
6	1998.08.25	29.86	88.31	5.8	15.0	Normal
7	2004.03.07	31.60	91.33	5.6	20.7	Strike-slip
8	1993.03.20	29.03	87.35	5.1	26.6	Vertical dip-slip
9	1993.03.20	28.87	87.64	6.2	15.0	Normal
10	2004.0824	32.50	92.28	5.5	12.0	Normal
11	2010.03.24	32.37	92.92	5.4	19.1	Normal oblique-slip
12	2010.03.24	32.37	92.89	5.7	17.8	Normal oblique-slip
13	1994.06.29	32.57	93.68	5.9	15.0	Normal
14	2009.07.24	31.05	86.10	5.8	28.1	Strike-slip
15	2004.03.27	33.87	89.19	5.0	18.4	Normal
16	2004.03.27	34.00	89.35	6.0	12.0	Normal

17	2003.07.07	34.67	89.59	5.8	33.0	Normal oblique-slip
18	2008.01.09	32.30	85.32	6.4	13.3	Normal
19	2008.01.16	32.35	85.29	5.9	12.0	Normal
20	2008.01.16	32.35	85.29	5.9	12.0	Normal
21	2001.03.05	34.47	86.76	5.9	15.0	Normal oblique-slip
22	2006.04.14	35.46	89.74	5.6	17.7	Normal
23	2006.04.19	31.61	90.67	5.7	23.2	Strike-slip
24	1997.11.08	35.33	86.96	7.5	16.4	Normal oblique-slip
25	2004.07.11	30.56	83.78	6.2	13.0	Normal
26	2005.04.07	30.24	83.77	6.3	12.0	Normal
27	2008.08.25	30.41	83.48	5.1	19.2	Normal
28	2008.08.25	30.85	83.72	5.0	23.7	Normal
29	2008.08.25	30.61	83.51	6.7	17.3	Normal
30	2008.09.25	30.66	83.69	6.0	21.2	Normal
31	2007.05.07	31.44	97.95	5.5	14.5	Normal
32	2002.06.04	30.13	81.25	5.6	15.0	Normal
33	2007.05.05	34.67	90.03	5.0	24.5	Strike-slip
34	2007.05.05	34.33	81.97	6.1	23.9	Normal
35	2008.10.06	29.56	90.53	5.2	13.6	Normal
36	2008.10.06	29.66	90.50	6.3	12.0	Normal
37	1990.01.14	37.60	92.10	6.0	15.0	Reverse
38	1990.04.26	36.01	100.27	6.2	15.0	Reverse
39	1990.04.26	36.25	100.57	6.4	15.0	Reverse
40	2000.09.12	35.50	99.48	6.1	15.0	Strike-slip
41	2001.11.14	35.80	92.91	7.8	15.0	Strike-slip
42	2001.11.18	35.94	93.51	5.6	15.0	Reverse
43	2001.11.19	35.83	93.52	5.3	15.0	Reverse
44	2003.04.17	37.53	96.45	6.3	16.0	Reverse
45	2004.03.16	37.60	96.56	5.1	13.0	Reverse
46	2004.05.10	37.55	96.58	5.5	12.0	Reverse
47	2007.02.02	37.87	91.85	5.4	20.2	Reverse
48	2008.11.10	37.51	95.75	6.3	27.2	Reverse
49	2009.08.28	37.64	95.76	6.3	12.0	Reverse
50	2009.08.28	37.75	95.76	5.0	17.0	Strike-slip
51	2009.11.04	37.65	95.83	5.1	14.5	Reverse
52	2010.04.14	33.18	96.53	6.1	17.9	Strike-slip
53	2010.04.13	33.05	96.79	6.9	15.7	Strike-slip
54	2010.05.29	33.20	96.28	5.8	20.8	Strike-slip

2.4 Seismics station in Tibet

As already mentioned, the Tibetan Plateau is one of the most active earthquake regions in the world. Earlier the distribution of seismic stations in Tibetan Plateau was very sparse, mainly because of its low population its history and harsh climatic conditions (Molnar and Tapponnier, 1978; Ni and York, 1978). At that time, the seismic data for the study of Tibetan earthquakes came from global data (Jin *et al*., 2009).

In 1990s, a large number of mobile and temporary broadband and short-period seismic stations, such as INDEPTH (International Deep Profiling of Tibet and the Himalaya) I, II, III were deployed by international cooperation projects at the central Tibetan Plateau (Haines *et al.*, 2003; Langin *et al.*, 2003; Zhao *al.*, 2001).

Nine digital seismic stations, which are operated by the China Earthquake Administration (CEA), were installed in Tibet since 2001. They are distributed in 9 different regions of Tibet as shown in Figure 2.6. All stations are equipped with Streckeisen Instruments (CTS-1 or CTS-2) and KS-2000 (Broadband Seismometer). Their basic parameters are given in Table 2.2.

Table 2.2 Parameters of the digital seismic station in Tibet*

Network Code	Station Code	Name of Station	Lat. (°N)	Lon. (°E)	Elevation (m)	Seismometer	Recorded Time
XZ	CAD	Changdu	31.14	97.17	3345	CTS-1	2001 to Now
XZ	CHY	Chayu				CTS-1	2007 to Now
XZ	GZE	Gaize				CTS-1	2007 to Now
XZ	LIZ	Linzhi				CTS-1	2007 to Now
XZ	LSA	Lhasa	29.73	91.10	3789	CTS-2	2001 to Now
XZ	NAQ	Naqu	31.45	92.09	4500	CTS-1	2001 to Now
XZ	PLA	Pulan				KS-2000	2007 to Now
XZ	RKZ	Rikaze				KS-2000	2007 to Now
XZ	SQHE	Shiquanhe				CTS-1	2007 to Now

Data obtained from CENC: http://www.csndmc.ac.c/newweb/network/csn_info.htm.
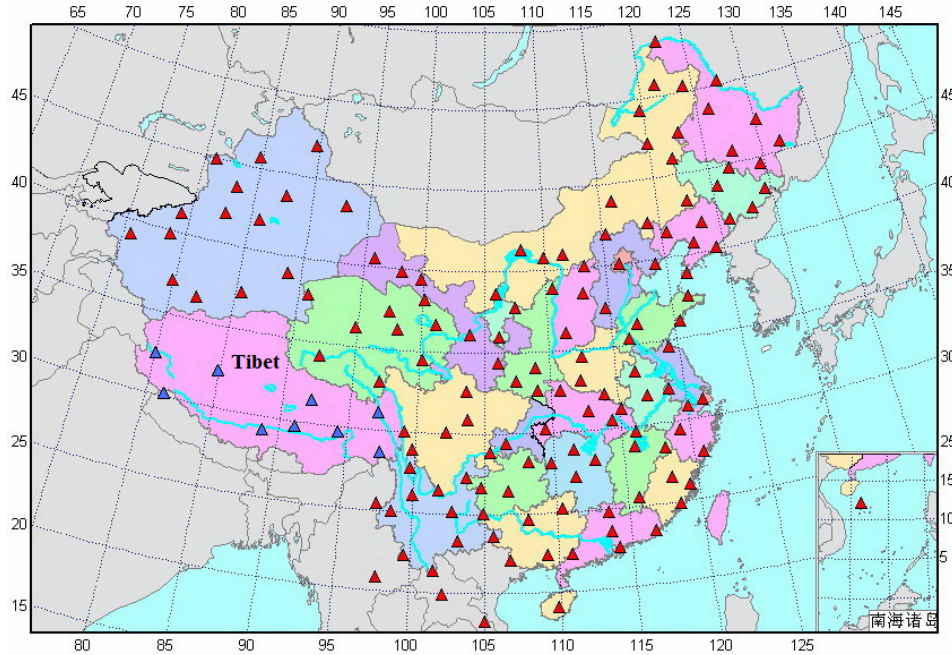
Figure 2.6 *Blue triangles indicate seismic station in Tibet. Modified from China Earthquake Network Center (CENC) http://www.csndmc.ac.cn/newweb/network/csn_stations_map_148.jpg).*

In addition, in a cooperative project between Tibet University and the University of Bergen, a small seismic network, called the Tibet University Seismic Network (TUB), was installed around Lhasa within an area of about 200 km, from August 2003 to 2005 (Figure 2.9). The equipment was provided by the Norwegian government through the University of Bergen. The network has currently 4 geophone stations that have generally been running stable. The TUB network detects earthquakes with magnitude greater than 2 around Lhasa. A total of about 6700 events were record by TUB for the time period 2004 to 2009 as shown in Figure 2.10. TUB has also recorded the magnitude 8.0 Whenchuan earthquake on 12 May, 2008, and the 6 October 2008 Damxung earthquake Mw6.3 as shown in Figures 2.7.
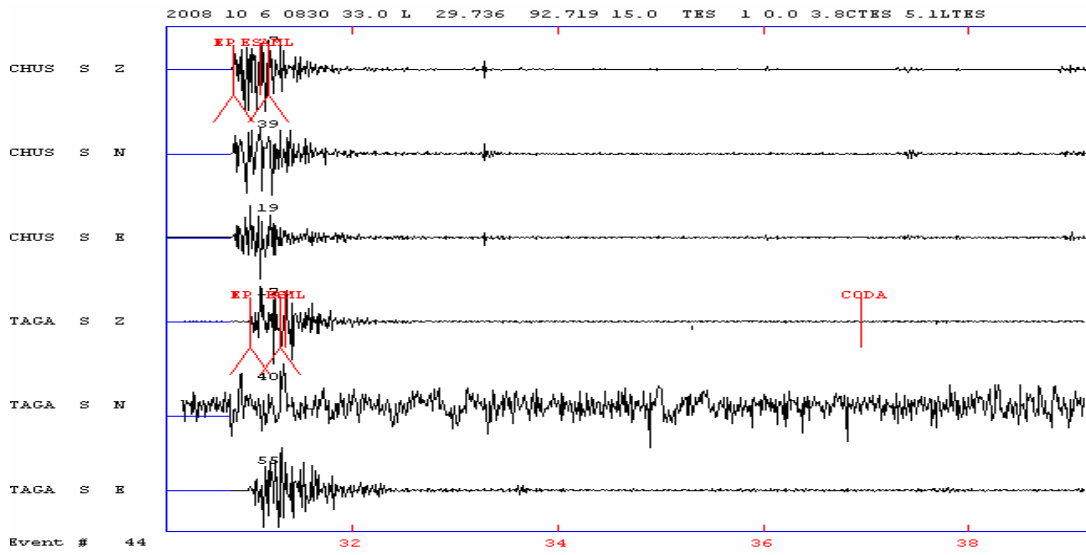
Figure 2.7 *Three-component seismograms of the 6 October 2008 Damxung earthquake recorded by both the CHUS and TAGA stations of the Tibet University Seismic Network (TUB). From Tibet University Seismic Network.*
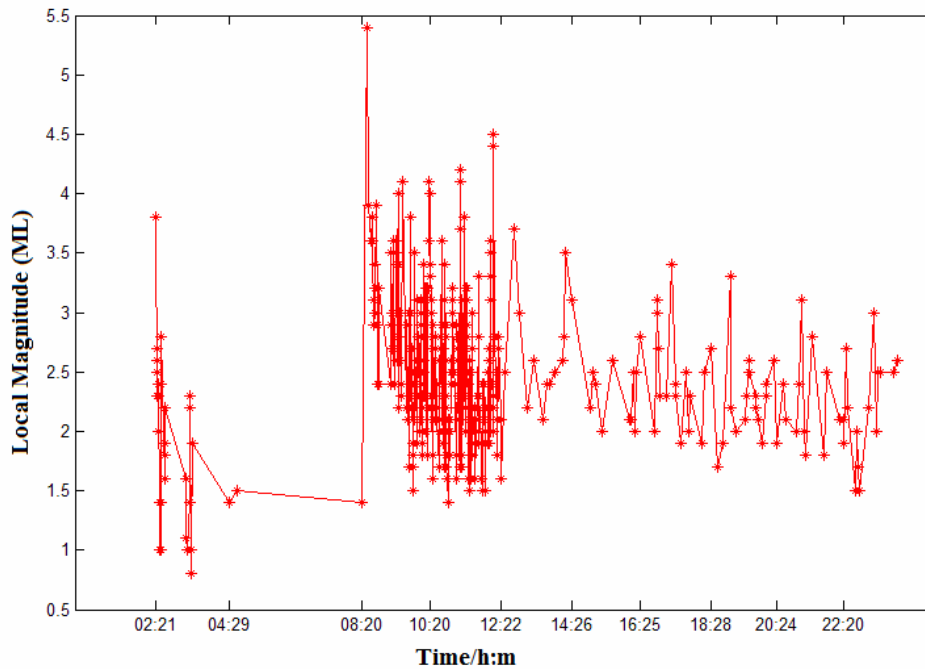
Figure 2.8 *Event magnitudes as a function of time for the 6 October, 2008 Damxung earthquake. Note that there is clear mainshock at around 8:20. Modified from Tibet Earthquake Administration (http: www.eq.xz.net).*

The 3-component geophones, 4.5 Hz, with digitizers of 16 or 24 bits, have been used in seismic network of TUB and use a GPS keeping the internal real time clock and the time stamping of the digitized data. The recorders are standard PCs using the SEISLOG recording system. Triggered data are collected at regular intervals (a week to a month) using a memory stick and all data is processed with SEISAN software (Ciren, 2006). More detailed information is shown in Table 2.3.

Table 2.3 Parameters of local seismic network of TUB

Station Name	Station Code	Latitude(°N)	Longitude(°E)	Seismometer	Installed Time
Jamag	JAMG	29.68	91.59	3-component , 4.5 Hz geophone	Aug 2003
Nhimo	NHIM	29.43	90.16	3-component , 4.5 Hz geophone	Aug 2003
Chudi	CHUD	29.70	91.12	3-component , 4.5 Hz geophone	Apr 2005
Chusang	CHUS	29.98	90.75	3-component , 4.5 Hz geophone	Aug 2005
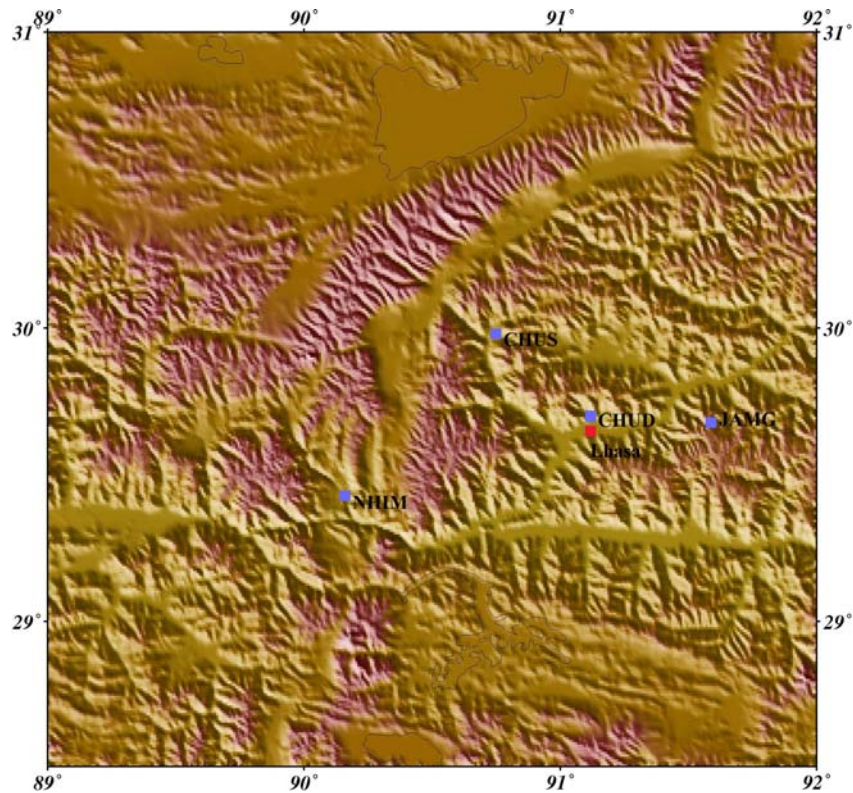
Figure 2.9 *Distribution of TUB network. Blue solid squares refer to stations.*
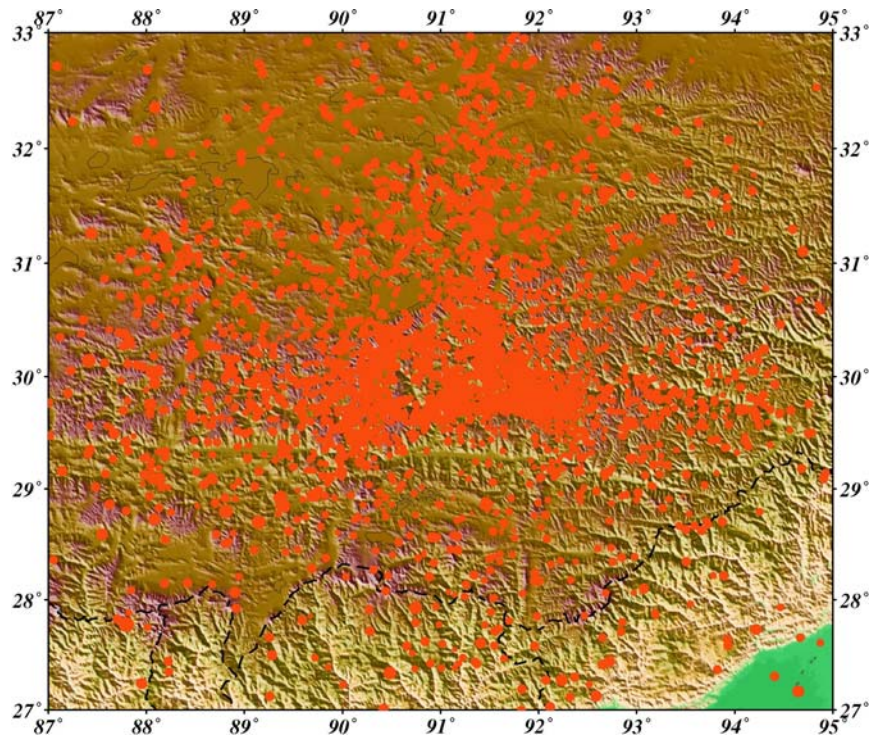
Figure 2.10 *Seismicity around Lhasa recorded by the TUB network between 2004 and 2009. Red circles represent events. The size of the solid circles is proportional to magnitudes.*

Chapter 3

The Damxung Earthquake, 2008

3.1 Seismic background

Damxung county is located north of Lhasa, at the junction of north and south Tibet. The terrain is sloping from northwest to southeast, around 160 km away from Lhasa. The average altitude is 4,300 m, covering an area of about 10,133 sq km and more than 40,000 people inhabit the area.

Based on the Technology and Archives (1982), a total of approximately 25 earthquakes (M≥4.7) occurred around Damxung in the period 1921 to 1982 (Table 3.1). Around half of them were distributed in the northern section of the Yadong-Gulu fault, such as the M 8.0 event on November 18, 1951 and M 7.5 event on August 18, 1952 as shown in Figure 3.1. In addition, a historic M 8.0 earthquake, which caused significant damage around Lhasa, also happened north of the village of Yangyi in Damxung, in 1411 (Technology and Archives, 1982; Wu *et al.*, 1992).
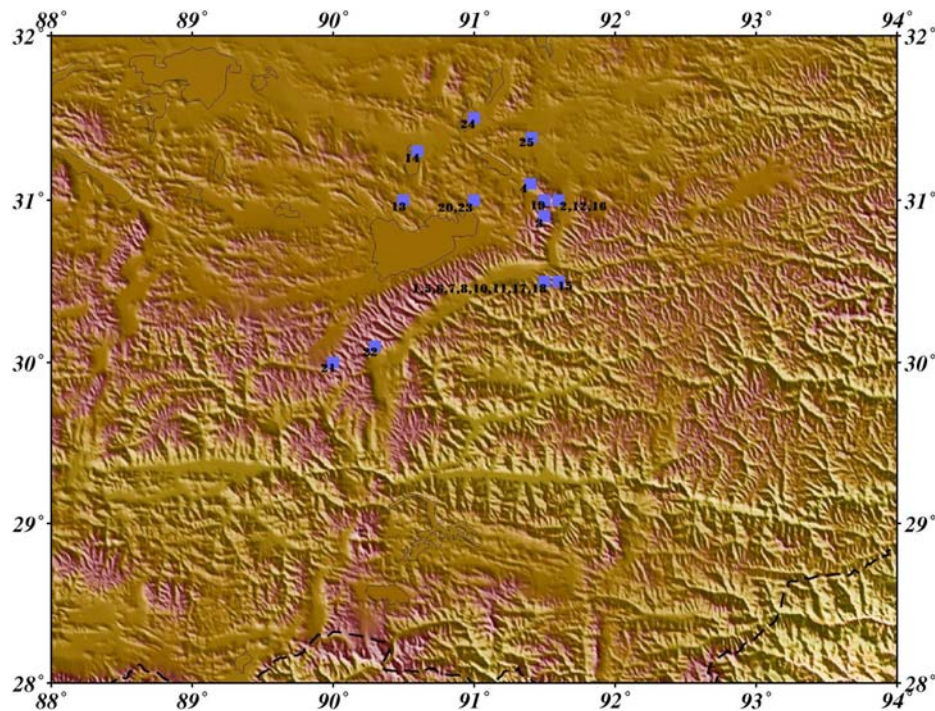
Figure 3.1 Epicentral map of events (M≥4.7). The number next to the filled square indicates events in Table 3.1.
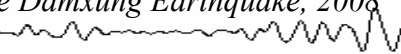
Table 3.1 Earthquakes (M ≥ 4.7) around Damxung from 1921 to 1982*.

Event	Date/y-m-d	Time/h-m-s	Latitude/deg	Longitude/deg	Magnitude
1	1925-01-12		30.5	91.5	6.5
2	1951-11-17	12-45-58	31.0	91.6	6.2
3	1951-11-18	17-26-37	30.9	91.5	6.8
4	1951-11-18	17-35-50	31.1	91.4	8.0
5	1951-11-18	19-22-56	30.5	91.5	5.7
6	1951-11-18	20-06-57	30.5	91.5	5.5
7	1951-11-19	01-46-35	30.5	91.5	5.5
8	1951-11-19	02-41-26	30.5	91.5	5.4
9	1951-11-19	08-26-43	31.0	91.6	5.0
10	1951-11-23	03-35-37	30.5	91.5	4.7
11	1951-11-23	12-11-46	30.5	91.5	5.0
12	1951-11-25	22-02-32	31.0	91.6	5.5
13	1951-12-08	04-52-50	31.0	90.5	5.5
14	1951-12-26	18-07-04	31.3	90.6	6.2
15	1952-03-15	02-19-57	30.5	91.6	5.0
16	1952-04-30	08-53-45	31.0	91.6	4.7
17	1952-06-02	18-08-23	30.5	91.5	5.3
18	1952-06-02	18-33-34	30.5	91.5	5.0
19	1952-08-18	00-02-11	31.0	91.5	7.5
20	1954-02-23	13-45-49	31.0	91.0	4.7
21	1955-12-19	06-37-45	30.0	90.0	5.0
22	1955-12-29	16-25-31	30.1	90.3	5.5
23	1957-04-22	13-29-01	31.0	91.0	4.8
24	1960-02-07	01-01-26	31.5	91.0	5.0
25	1972-07-23	00-41-02	31.38	91.41	5.9

* *Data obtained from Technology and Archives (1982).*

3.2 The Damxung earthquake

On 6 October 2008, an M_w6.3 earthquake occurred at the village of Yangyi, in the south of Damxung. The epicenter was approximately 77 km northwest of Lhasa. The source parameters given by the China Earthquake Network Center (CENC) are origin time, 8:30 (UTC), epicenter, 29.8ºN, 90.3ºE (Figure 3.2); depth, 8.0 km and M_w=6.3. The mechanism was given as oblique normal with a right-lateral strike slip component (Qiao *et al.*, 2010). More source parameters are given by other earthquake agencies as shown in Table 3.2.

**Table 3.2** Parameters of the October 6, 2008, Damxung earthquake.

Date(y. m. d)	Time (h : m :s)	Epicenter(º)	Depth (km)	Magnitude	Agency
2008.10.06	08:30:46	29.761N, 90.320E	12.0	Mw 6.4	USGS NEIC
2008.10.06	08:30:46	29.80N, 90.35E	12.0	Mw 6.3/Ms6.2/Mb6.0	IRIS
2008.10.06	08:30:52.5	29.64N, 90.46E	12.0	Mw 6.4/Ms 6.6/Mb 6.6	GCC
2008.10.06	08:30:46	29.704N, 90.274E	10.0	Mw 6.3	USGS CMT
2008.10.06	08:30:46	29.702N, 90.269E	7.0	Mw 6.1	USGS BWMT

Figure 3.2 shows that the mainshock occurred in the Yadong-Gulu rift, which has an approximate S-N extension, around 500 km between Yadong in the Himalayas and north of Gulu (Armijo *et al.*, 1986; Chen *et al.*, 2004; Cogan *et al.*, 1998; Mercier *et al.*, 1987; Ni and Barazang, 1984; Wu *et al.*, 2010; Zhao *et al.*, 2001). The rift consists of a few active grabens or half-grabens (Wu *et al.*, 2010). At the western end of the Damxung-Yangbajain rift, which is 120 km long and 10-25 km wide and situated in the central-north Yadong-Gulu rift, the most famous late Cenozoic extensional tectonic feature as well as one of the most active faults in the Tibetan Plateau is found. The epicenter of the 2008 Damxung earthquake is situated between the northern Nyainqentanglha Mountains (NQTGLM) and the southern Yarlung Tsangpo suture. In the past, a number of moderate or great events were felt north of the epicenter as described in the previous section.

Based on (Wu *et al.*, 2010; Wu *et al.*, 2009) and Tibet Earthquake Administration (http://www.eq-xz.net/newweb/shownews.asp?id=314), the intensity of this earthquake

was VIII, even reaching to IX at the epicenter as shown in Figure 3.4. Most of the houses surrounding the area of the epicenter are civil structures built with stones or unfired adobe bricks with slurry to paste the walls, and with roofs made of wooden trusses and straw cemented with mud (Figure 3.5). Without any earthquake resistant features, 147 houses collapsed (http://baike.baidu.com/view/2406293.html#4), and 10 people were killed and 60 were injured (Wu, Ye, Barosh and Wu, 2010).

The earthquake was strongly felt in the adjacent regions of Damxung, for example, Lhasa, Nihmo, Shigaze etc. Buildings did not collapse at these locations, but minor damages were observed.
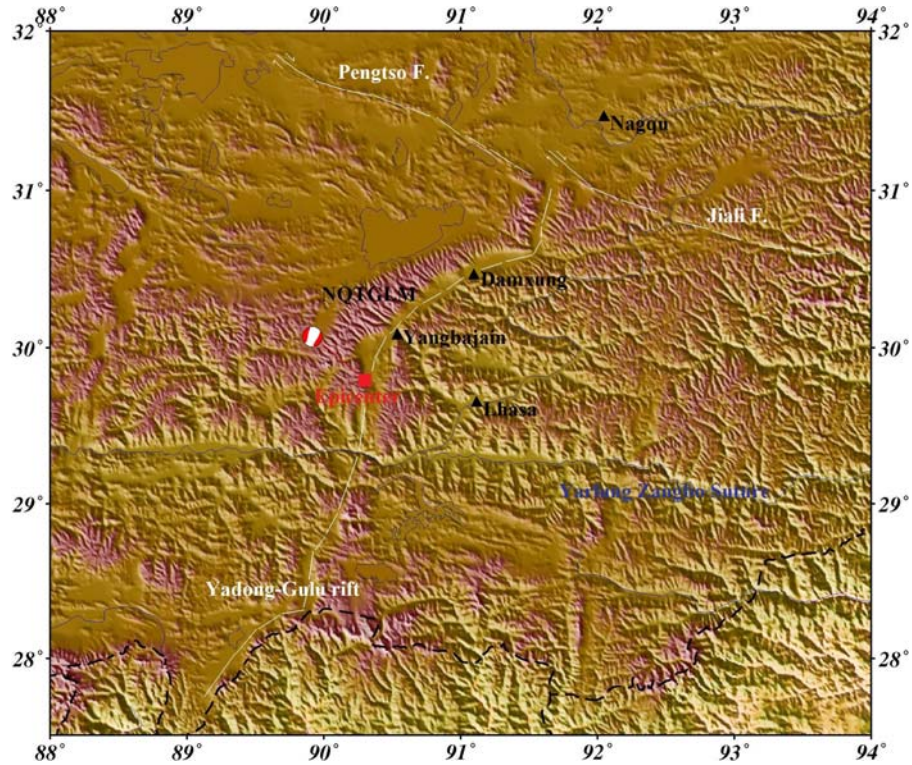
Figure 3.2 *Distribution of topography and active tectonics around the study area. The focal mechanism is from GCMT (http://www.globalcmt.org/CMTsearch.html).*

Based on data from the Tibet Earthquake Administration (http:www.eq-xz.net), the main shock was followed by a total of 1044 aftershocks until October 11, 2008 at 19:00, including 2 events (M=5.0 -5.9), 1 event (M=4.0 - 4.9), 27 events (M=3.0 - 3.9), 169

events (M=2.0 - 2.9), 645 events (M=1.0 - 1.9) and 200 events (M=0.0 - 0.9). Figure 3.3 shows the distribution of the mainshock as well as many of the aftershocks.

   A series of earthquakes has occurred in the area since then. For example, magnitude 3.2 earthquakes were felt at the location of 29.8º N, 90.4º E on November 20, 2008 at 18:42 and on September 7, 2009 at 22:17 respectively. On May 14, 2010 at 22:46, a magnitude 4.7 earthquake occurred at the location of 29.7º N, 90.4º E, on November 30, 2010 at 16:39, a magnitude 5.2 earthquake happened at the location of 29.8º N, 90.4º E. Finally on December 03, 2010 at 21:14, a magnitude 3.1 earthquake occurred at the location of 29.9º N, 90.4ºE.
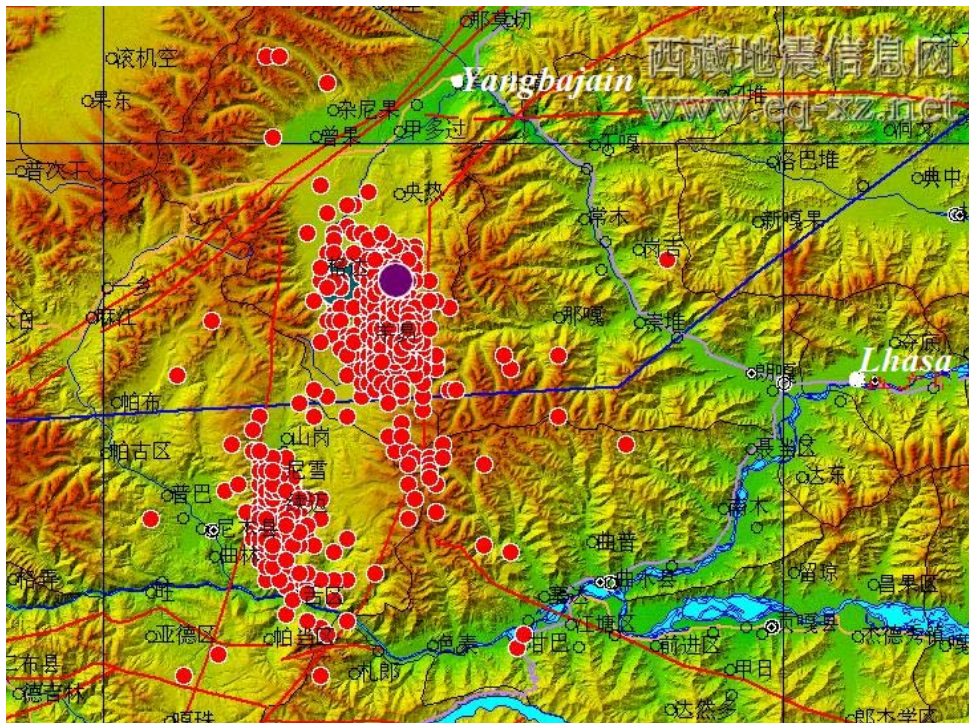
Figure 3.3 *Map of intensity distribution of the 6 Oct, 2008 Damxung earthquake. The purple circle indicates the epicenter. Modified from: http://www.cea.gov.cn/manage/html/8a85878816 32fa5c0116674a018300cf/_content/08_10/28/1225165068499.html.*
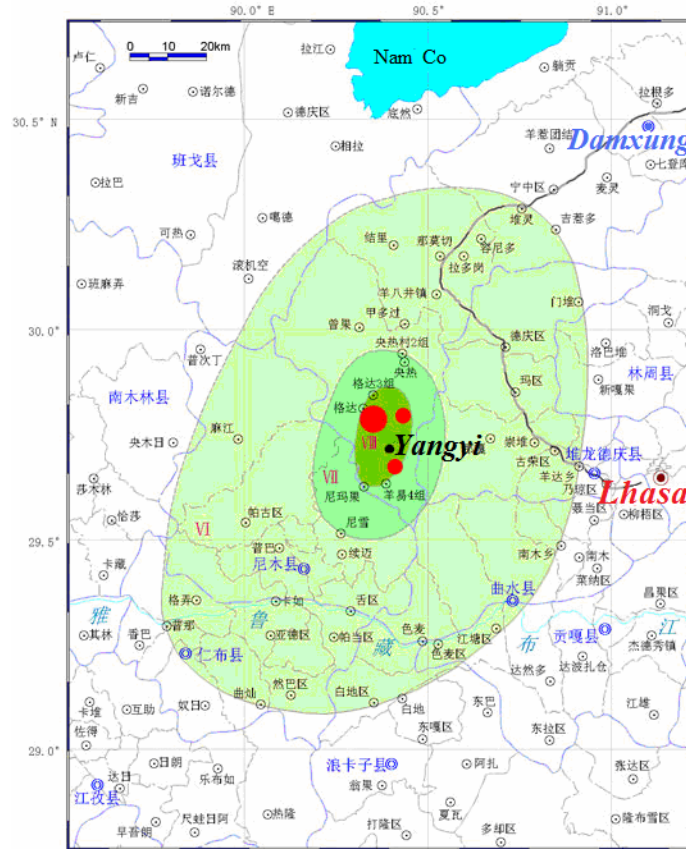
Figure 3.4 *Map of the source region of the 2008 Damxung earthquake. The large purple circle is the mainshock epicenter; the other red dots are aftershocks, up till 19:00 on October 11, 2008. VI, VII and VIII represent intensity. Modified from: http://www.eq-xz.net/newweb./shownews .asp?id=314).*

Figure 3.5 *A damaged house in Gedar village, Damxung, Tibet, on 6 October, 2008. From Xinhua news agency.*

Chapter **4**

Teleseismic Moment Tensor Inversion

The teleseismic body wave inversion methodology technique was developed by Kikuchi and Kanamori (1982, 1986 and 1991) to determine the earthquake source parameters and the kinematic rupture process of the fault. Similar technique have been successfully applied to many earthquakes (Barker and Langston, 1981; Barker and Langston, 1983; Estabrook, 1999; Hartzell and Heaton, 1983).

In the following, I will use the Kikuchi and Kanamori's inversion method with their algorithm (2003) to determine the focal mechanism solution, seismic moments and the depth of the 2008 Damxung and 1992 Nyimo earthquakes, respectively.

4.1 Inversion method

If the hypocenter location and the Green's function of corresponding crustal model are known, the observed seismograms can be used for linear moment tensor inversion(Yuntai *et al.*, 2000).

The inversion problem can be given in simple matrix form

$$\mathbf{u} = \mathbf{Gm} \qquad (4.1)$$

where **u** is a vector composed of observed seismograms for each channel; **G** is a matrix which has as many rows as observed seismograms and as many columns as moment tensor components that are the Green's functions; **m** is the model vector containing the moment tensor elements which has six independent moment tensor components (Havskov and Ottemöller, 2010; Lay and Wallace, 1995; Stein and Wysession, 2003). Hence, equation 4.1 can be expressed as follows.

$$
\begin{bmatrix} u_1 \\ u_2 \\ . \\ . \\ . \\ u_n \end{bmatrix} = \begin{bmatrix} G_{11} & G_{12} & G_{13} & G_{14} & G_{15} & G_{16} \\ G_{21} & G_{22} & G_{23} & G_{24} & G_{25} & G_{26} \\ . & . & . & . & . & . \\ . & . & . & . & . & . \\ . & . & . & . & . & . \\ G_{n1} & G_{n2} & G_{n3} & G_{n4} & G_{n5} & G_{n6} \end{bmatrix} \begin{bmatrix} m_1 \\ m_2 \\ m_3 \\ m_4 \\ m_5 \\ m_6 \end{bmatrix}
\qquad (4.2)
$$

In theory, in order to solve 6 unknown moment tensor components (m_1-m_6), as long as there are at least 6 observed seismograms, the 6 unknown moment tensor components (m_1-m_6) can be solved. In practice, we have more than 6 observed seismograms and the G matrix is not square and the problem of inversion is over determined. Then **m** would be determined by using a least squares method, i.e., **m** is calculated to obtain the smallest misfit between observed and synthetic seismograms (Cui-Ping *et al.*, 2008; Havskov and Ottemöller, 2010).

The model vector **m** can be inverted for in a least square sense through

$$
\begin{aligned}
\mathbf{m} &= \mathbf{(G^T G)^{-1} G^T u} \\
&= \mathbf{G^{-g} \ u}
\end{aligned}
\qquad (4.3)
$$

where $\mathbf{(G^T G)^{-1} G^T = G^{-g}}$ is called the generalized inverse of G (Lay and Wallace, 1995; Stein and Wysession, 2003).

4.2 Data processing

The three-component (BHZ, BHE,BHN) broadband teleseismic seismograms of the 6 October, 2008 Damxung earthquake used in the inversion were collected from 26 stations of the Global Seismographic Network (GSN) with Wilber II of IRIS on the web site of IRIS-DMC (http://www.iris.edu/dms/wilber.htm). Teleseismic distances in the range between 30° and 90° were used, in order to avoid upper mantle and core triplications and to limit the path length within the crust (Barker and Langston, 1981; Burdick and Mellman, 1976). Using the software, *rdseed*, the waveform data in seed

format were converted to sac binary with the " R" and "d" option. The station coverage is shown in Figure 4.1.

Before pursuing the inversion problem by the software of Kikuchi and Kanamori (2003), I completed several preparatory steps.

- The Seismic Analysis Code (SAC), used to prepare the data, had to be installed in my computer.
- *rdseed* software, used to convert the waveform data from seed to sac binary, was required.

- Two input files, *hypo* and *sacmacros*, (below) were also required.

```
hypo
----------------------------
0810060830 Xizang
 29.81  90.35  12  8 30 45 0 30 90
--------------------------------------------------
```

```
sacmacro
------------------------
r *.*.*.??E
w alpha append .A
r *.*.*.??N
w alpha append .A
r *.*.*.??Z
w alpha append .A
------------------------
```

- Reset of the parameter values in program *mk_conv.farm.pl*. For example in this work, I used the value of the parameters: *du=720, pre_ev=20, sample=1.0. low_pass_co=0.5 and high_pass_co=0.01*. Where *du* is duration, *pre_ev* is duration of the data before the P time, *sample* is the sampling interval in sec, *low_pass_co* is the cut-off frequency of the low-pass filter, and *high_pass_co* is the cut-off frequency of the high-pass filter.
- Running the program *mk_conv.pl* to make *response* file and *i_conv.farm*.
- Running *conv.sac.farm* program to produce *fort.22* as: *conv.sac.far < i_conv.farm*. where *fort.22* is a file with data from all station.

According to my own experience, the program, *conv.sac.farm*, usually does not run successfully the first time. Because of that, we should check the contents of *response* and

i_conv.farm, as well as the data in *sac* format. Then stations not displayed in *response* and *i_conv.farm*, should be excluded from the data of *sac* format.

- Running the *rotSH* program to rotate the data in sac format of earthquake to *fort.1* as : *rotSH.* Sometimes, the *rotSH* program does not run successfully the first time either. We should remove some incorrect data in *fort.22*.
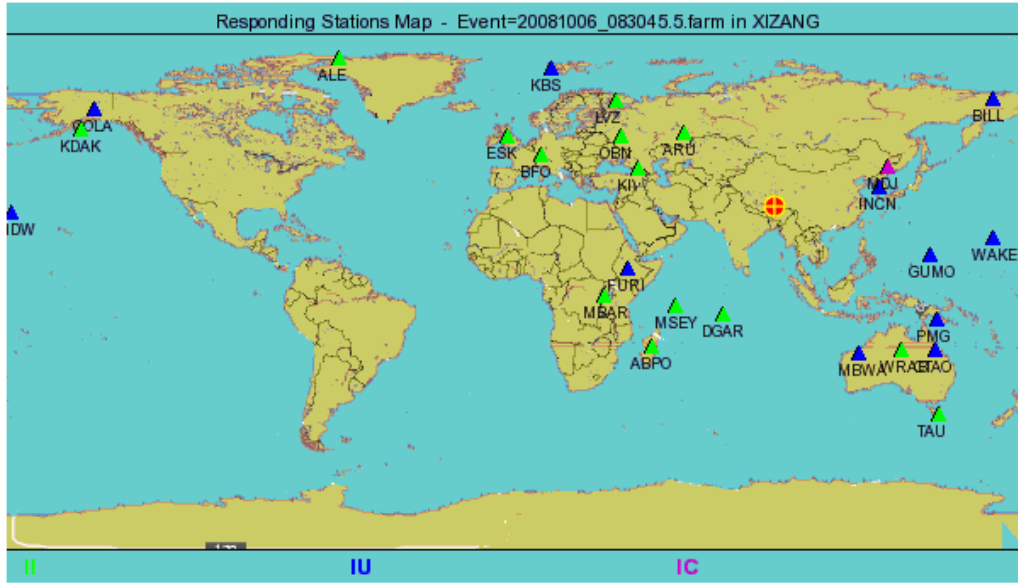
Figure 4.1 *Distribution of seismic stations used in the moment tensor inversion. Green triangles represent the Global Seismograph Network (GSN – IRIS/IDA), the purple triangle refers to New China Digital Seismograph Network (NCDSN), and the blue triangles represent Global Seismograph Network (GSN – IRIS/USGS). The letters below triangles indicate station codes. The red filled circle indicates the epicenter of the 6 October, 2008 Damxung event.*

4.3 Inversion of the 2008 Damxung earthquake

26 P and 14 SH waveforms (Table 4.2), which had good agreement between observed and synthetic seismograms or a good signal to noise ratio, were chosen for the inversion. Station locations and parameters used in this inversion are listed in Table 4.1 and 4.2, respectively.

Table 4.1 Location of station used in the inversion

Network	Station Code	Lat. (°)	Lon. (°)	Elevation (m)	Location
GSN-IRIS/IDA	ABPO	19.02	47.23	1528.00	Ambohimpanompo, Madagascar
GSN-IRIS/IDA	ALE	80.50	-62.35	60.00	Alert, N.W.T., Canada
GSN-IRIS/INA	ARU	56.43	58.56	250.00	Arti, Russia
GSN-IRIS/IDA	BFO	48.33	8.33	589.00	Black Forest Observatory, Schiltach, Germany
GSN – IRIS/USGS	BILL	68.07	166.45	320.00	Bilibino, Russia
GSN – IRIS/USGS	COLA	64.87	-147.86	200.00	College Outpost, Alaska, USA
GSN – IRIS/USGS	CTAO	-20.09	146.25	357.00	Charters Towers, Australia
GSN-IRIS/IDA	DGAR	-7.41	72.45	1.00	Diego Garcia, Chagos Islands, Indian Ocean
GSN-IRIS/IDA	ESK	55.32	-3.21	242.00	Eskdalemuir, Scotland, UK
GSN – IRIS/USGS	FURI	8.90	38.69	2570.00	Mt. Furi, Ethiopia
GSN – IRIS/USGS	GUMO	13.59	144.87	170.00	Guam, Mariana Islands
GSN – IRIS/USGS	INCN	37.48	126.62	80.00	Inchon, Republic of Korea
GSN – IRIS/USGS	KBS	78.92	11.94	90.00	Ny-Alesund, Spitzbergen, Norway
GSN-IRIS/IDA	KDAK	57.78	-152.58	152.00	Kodiak Island, Alaska, USA
GSN-IRIS/IDA	KIV	43.96	42.69	1054.00	Kislovodsk, Russia
GSN-IRIS/IDA	LVZ	67.90	34.65	630.00	Lovozero, Russia
GSN-IRIS/IDA	MBAR	-0.60	30.74	1390.00	Mbarara, Uganda
GSN – IRIS/USGS	MBWA	-21.16	119.73	190.00	Marble Bar, Western Australia
NCDSN	MDJ	44.62	129.59	270.00	Mudanjiang, Heilongjiang Province, China
GSN – IRIS/USGS	MIDW	28.22	-177.37	20.00	Midway Island, USA
GSN-IRIS/INA	MSEY	-4.67	55.48	475.00	Mahe, Seychelles
GSN-IRIS/IDA	OBN	55.11	36.57	160.00	Obninsk, Russia
GSN – IRIS/USGS	PMG	-9.40	147.16	90.00	Port Moresby, New Guinea
GSN-IRIS/INA	TAU	-42.91	147.32	132.00	Hobart, Tasmania, Australia
GSN – IRIS/USGS	WAKE	19.28	166.65	20.00	Wake Island
GSN-IRIS/IDA	WRAB	-19.93	134.36	366.00	Tennant Creek, NT, Australia

Table 4.2 Station Parameters used in the inversion.

Station Code	Distance (º)	Azimuth (º)	Back Azimuth (º)	Phase
ABPO	63.9	-134.1	41.2	P, SH
ALE	67.1	-3.7	25.6	P , SH
ARU	34.8	-30.8	126.6	P
BFO	63.3	-47.5	74.4	P, SH
BILL	57.5	25.5	-90.5	P, SH
COLA	75.4	21.9	-49.7	P, SH
CTAO	73.2	125.7	-48.6	P, SH
DGAR	40.8	-152.3	24.0	P
ESK	68.0	-37.8	69.3	P, SH
FURI	52.5	-102.4	59.1	P
GUMO	52.7	95.5	-62.7	P
INCN	31.0	65.9	-93.5	P
KBS	58.7	-12.8	95.1	P, SH
KDAK	78.1	29.0	-52.2	P, SH
KIV	40.1	-55.8	94.3	P
LVZ	50.0	-24.0	110.4	P, SH
MBAR	64.2	-106.8	56.2	P, SH
MBWA	58.0	147.5	-30.0	P
MDJ	34.2	53.3	-102.2	P, SH
MIDW	78.3	64.1	78.3	P
MSEY	47.9	-129.9	41.9	P
OBN	45.6	-40.3	101.0	P, SH
PMG	67.1	116.4	-52.0	P, SH
TAU	89.3	142.1	-46.7	P
WAKE	69.1	79.2	-64.5	P
WRAB	65.1	134.1	-41.5	P

4.3.1 Calculation of Green's function

The teleseismic data and seismic velocity structure of Jeffreys and Bullen's seismic velocity model (J-B model) (Table 4.3), as well as the file, *i_green*, as given below are input parameters to the program of Kikuchi and Kanamori (2003). Use the command, *green< i_green*, to calculate Green's functions (synthetic seismograms).

i_ green

```
-------------------------------------
 256  0.5  h   5.0   1  1  90
-------------------------------------
```

Where assuming the *h* value is 10.0 km. See Kikuchi and Kanamori (2003) for meaning of the parameters in *i_green*.

**Table 4.3** Crustal velocity structure model and density

Depth (km)	V_P (km/sec)	V_S (km/sec)	ρ(kg/m^3) $\times 10^3$
Near Source Crustal Structure (J-B model)			
0.0	8.10	4.68	3.30
15.0	5.57	3.36	2.65
18.0	6.50	3.74	2.87
Near Receiver Crustal Structure (J-B model)			
0.0	8.10	4.68	3.30
15.0	5.57	3.36	2.65
18.0	6.50	3.74	2.87
PP Bounce Point Structure (J-B model)			
0.0	6.50	3.74	2.87

Data obtained from (Kikuchi and Kanamori, 2003)

4.3.2 Moment tensor inversion

Similarly, the seismic data and the calculated results of Green's function as well as the *i_inversion* file as shown below were used for input parameters to the software of Kikuchi and Kanamori (2003) to do moment tensor inversion with command, *inversion < i_inversion*, with a triangular function as the source time function. The focal mechanism solution was obtained by minimizing the difference between synthetic and observed seismograms.
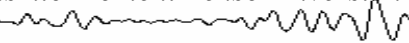
i_inversion

Damxung,Tibet 06/10/08

80 4

3 6 12

1

20

98 1 1 1 0 0 0 1 1 0 0 0 1 1 1 0 0 0 0 0 0

  0 0 1 0 0 0 0 1 1 1 1 0 0 1 0 0 1 1 1 0

  0 0 1 0 1 1 0 0 0 1 0 0 0 1 0 0 1 1 1 0

  0 1 1 0 0 0 0 0 1 0 0 0 1 0 0 0 1 0 0 1

  1 0 0 1 1 0 1 1 1 1 0 0 0 0 0 1 0 1

-20 0 1

0 5 1 1

See Kikuchi and Kanamori (2003) for meaning of the parameters in *i_inversion.*

4.3.3 Plot the data in fort.4

Finally, the inversion results and the file, *i_graphics*, as given below are used as input parameters to the program of Kikuchi and Kanamori (2003), to plot calculated results as shown in Figure 4.2 with the command, *graphics < i_graphics*.
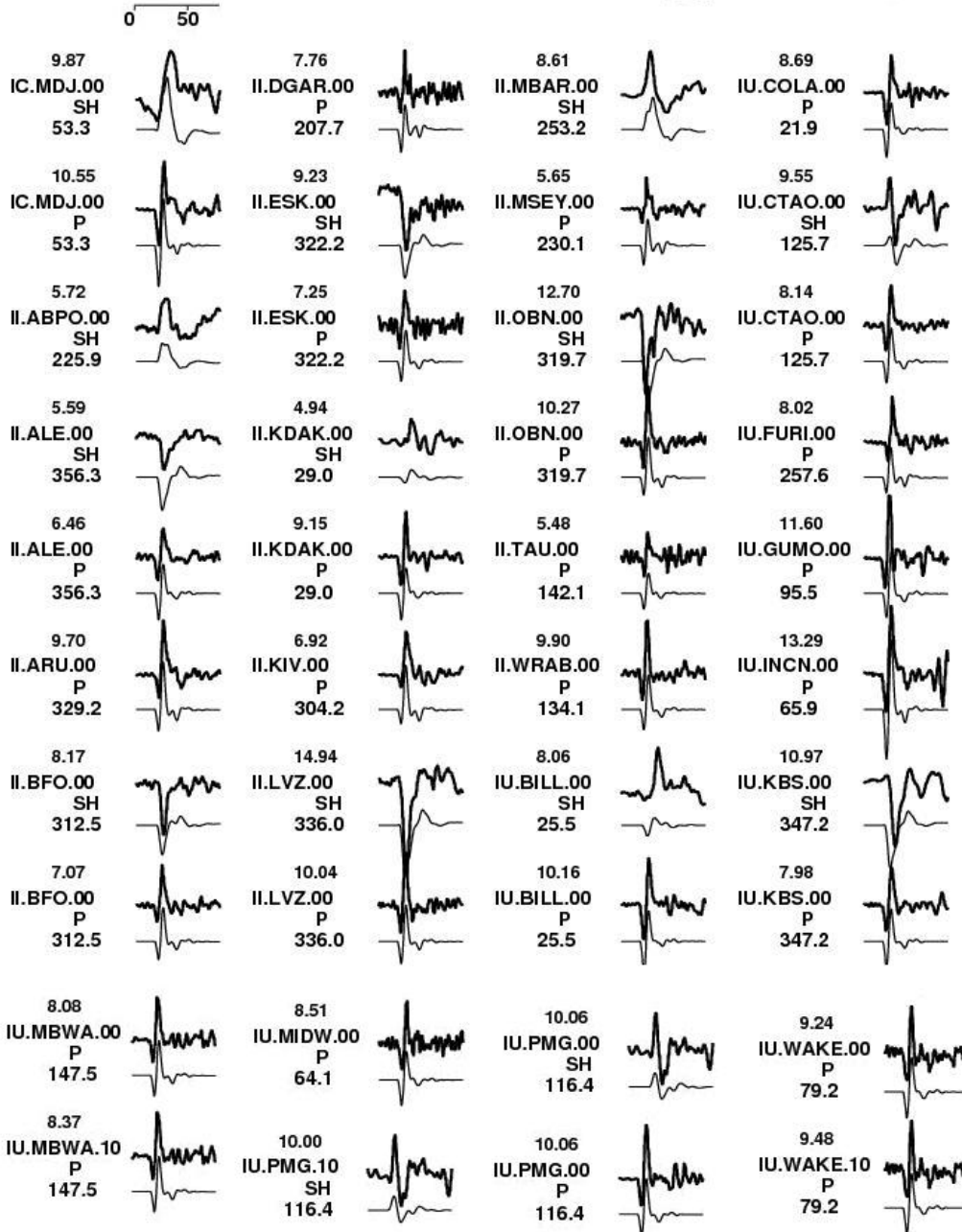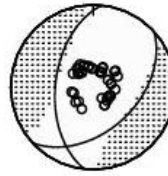

i_graphics

 50.0 3 1.0 0 0.2

1 1 1

See Kikuchi and Kanamori (2003) for meaning of the parameters in *i_graphics.*

Figure 4.2 *Top trace of each seismogram pair is the observed seismograms and the bottom trace is synthetic. The number above the station code and below the phase code indicates peak-to-peak amplitude in microns and the station azimuth, respectively. Source time function and focal mechanism are shown in the right corner and middle of the page respectively, obtained by inversion of teleseismic 26-P and 14-SH waveforms with J-B velocity model (Table 4.3) for the 6 October 2008 Damxung mainshock.*

In the following, the velocity and density model near the source, I used the local crustal structure model which is divided into 6 layers with thickness of 55 km. The receiver structure at all stations used J-B model (Table 4.3).

The P-wave velocity structure and crustal density beneath the Lhasa block were obtained from INDEPTH III (Figure 4.3) seismic data by Haines, *et al.* (2003). Based on the ratio of P-wave to S- wave velocity of $V_P=1.73 \ V_S$ (Wang *et al.,* 2008) beneath the Lhasa block are calculated the corresponding S-wave velocity as shown in Table 4.4.
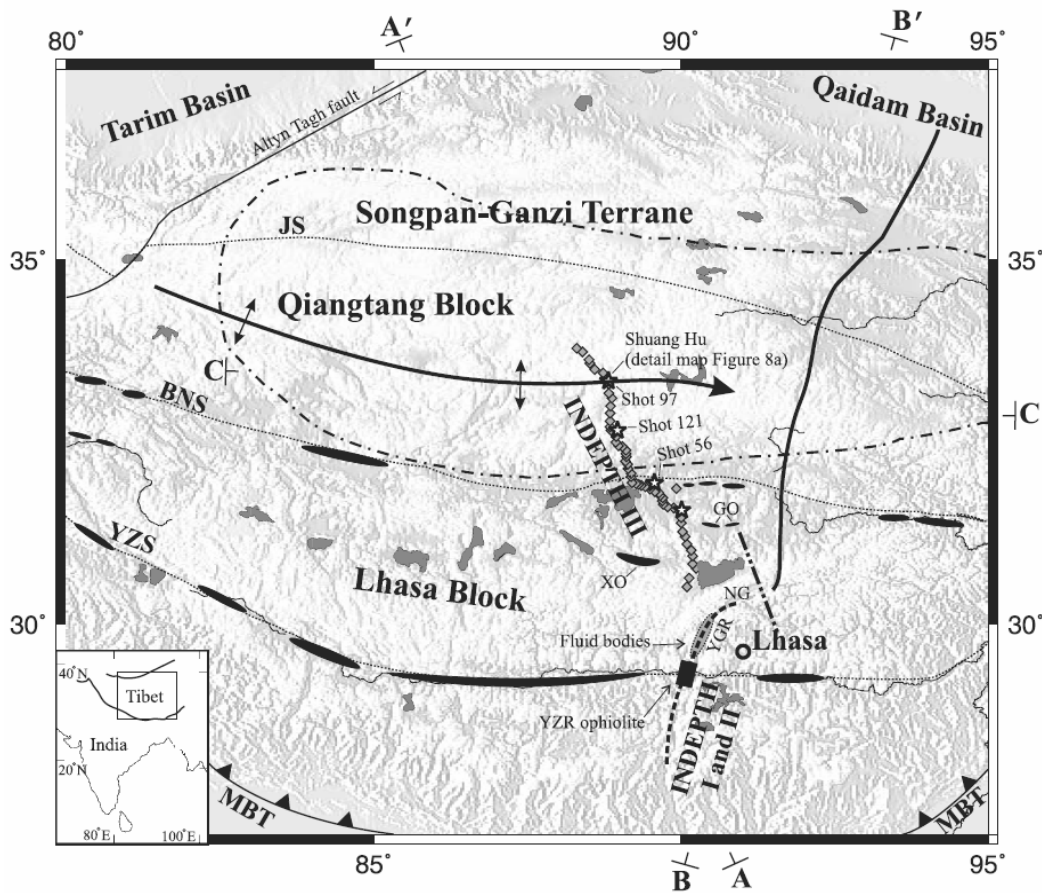

Figure 4.3 *Map of my study region, showing the INDEPTH I+II and INDEPETH III profiles. The epicenter of the Damgxung earthquake is roughly at YGR area. Figure from Hain et al. (2003).*

Table 4.4 Crustal velocity structure model and density

| Depth (km)	V_P (km/sec)	V_S (km/sec)	$\rho(kg/m^3) \times 10^3$
Near Source Crustal Structure (beneath the Lhasa block)			
0-5.0	5.00	2.89	2.57
5-20	6.00	3.47	2.71
20-35	6.25	3.61	2.80
35-45	6.50	3.76	2.93
45-55	6.73	3.89	3.03
55 >	7.10	4.10	3.14
Near Receiver Crustal Structure (J-B model)			
0.0	8.10	4.68	3.30
15.0	5.57	3.36	2.65
18.0	6.50	3.74	2.87
PP Bounce Point Structure (J-B model)			
0.0	6.50	3.74	2.87

Since the inversion result depends on the depth of the reference point, *h* (see section 4.3.1: *i_green*), where *h* is the depth of the reference point for calculation synthetic data with Green's function and the values of depth stand for the depth of the source. If the inversion is carried out at the wrong depth, the resulting mechanism will certainly be incorrect. Therefore, in order to obtain an appropriate depth, I determined the depth by inverting for a whole range of depths, typically between 1 and 20 km by 1 km intervals and other parameters were kept the same setting value and then choosing the depth with minimal variance was chosen.

I found the *h* value has an impact on the result of focal mechanism as shown in Figure 4.4 and the appropriate depth is approximately 11 km, since the corresponding variance is the smallest.
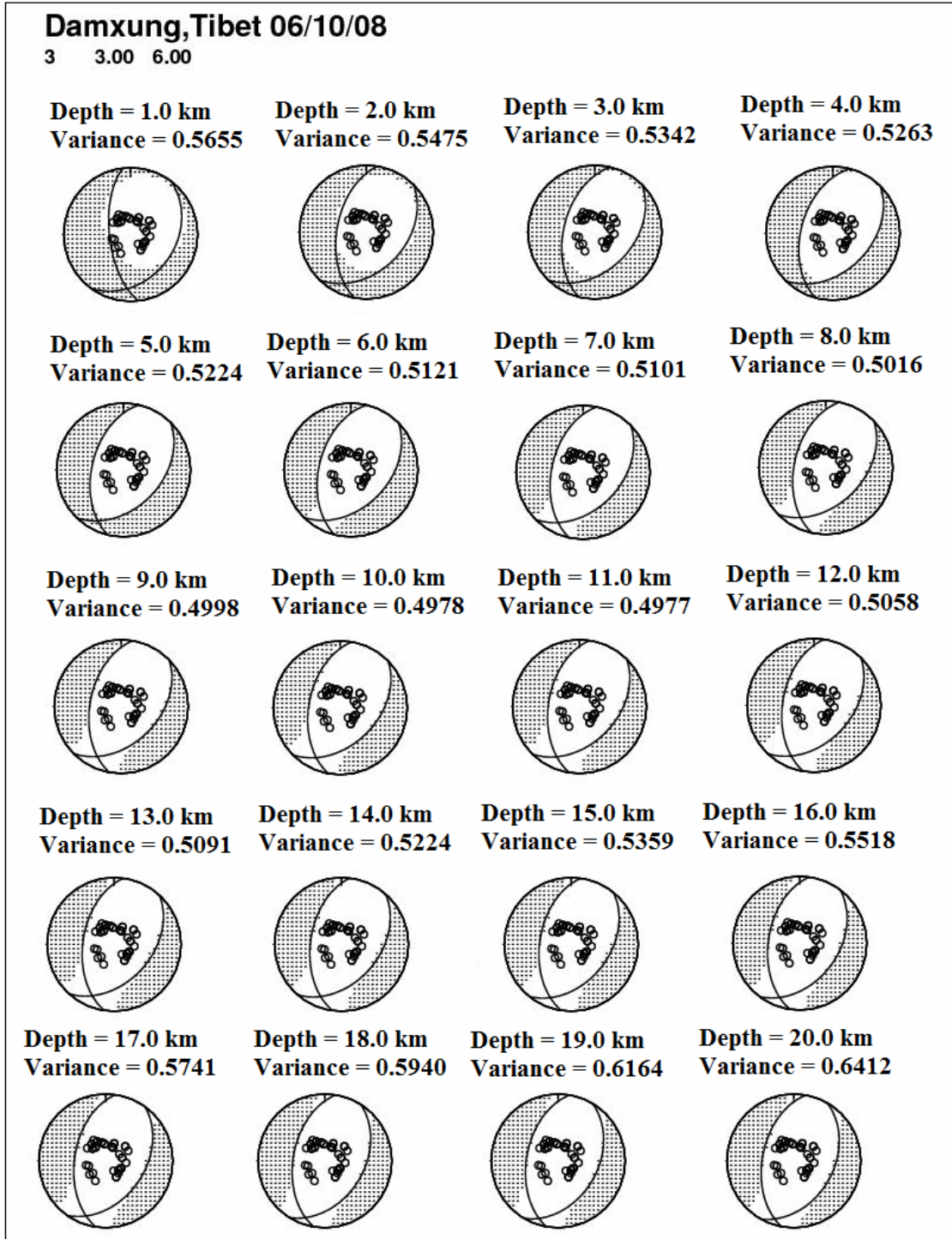
Figure 4.4 *An example of focal mechanisms for the 6 October 2008 Damxung mainshock with different depth values. It obtained by triangular source time function and local velocity model. Depth and variance are shown on each solution.*

Furthermore, I tried different models of source time function, e.g. impulse function, trapezoid function and cosine-tapere ramp function and also various *h* values in the attempt to find the best focal mechanism solution, as shown in Figures 4.5a - 4.5c.
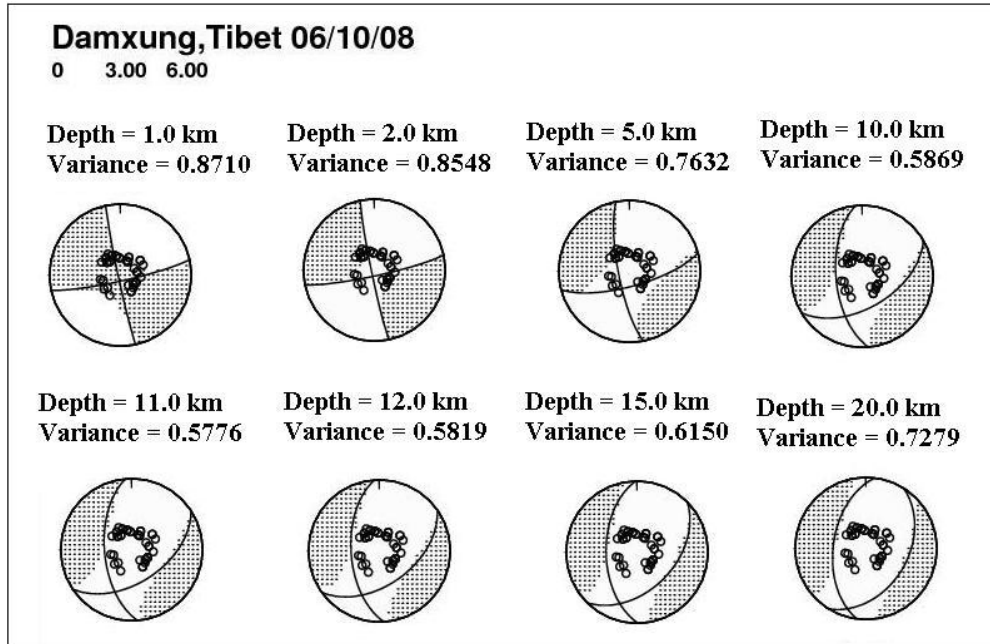
Figure 4.5a An example of focal mechanism for the 6 October 2008 Damxung earthquake with impulse source time function and local velocity model. Depth and variance are shown on each solution.

Damxung,Tibet 06/10/08
1   3.00 6.00

Depth = 1.0 km
Variance = 0.5679

Depth = 2.0 km
Variance = 0.5415

Depth = 5.0 km
Variance = 0.5092

Depth = 10.0 km
Variance = 0.5079

Depth = 11.0 km
Variance = 0.5091

Depth = 12.0 km
Variance = 0.5178

Depth = 15.0 km
Variance = 0.5479

Depth = 20.km
Variance = 0.6299
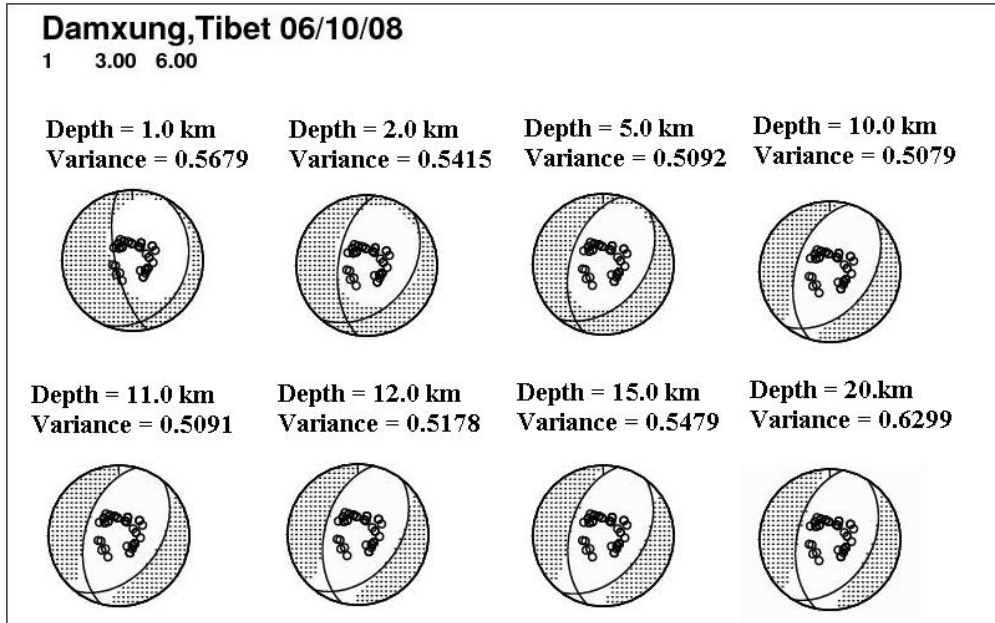
Figure 4.5b An example of focal mechanism for the 6 October 2008 Damxung earthquake with trapezoid source time function and local velocity model. Depth and variance are shown on each solution.

Damxung,Tibet 06/10/08
2   3.00 6.00

Depth = 1.0 km
Variance = 0.5707

Depth = 2.0 km
Variance = 0.5458

Depth = 5.0 km
Variance = 0.5141

Depth = 10.0 km
Variance = 0.5061

Depth = 11.0 km
Variance = 0.5072

Depth = 12.0 km
Variance = 0.5161

Depth = 15.0 km
Variance = 0.5463

Depth = 20.0 km
Variance = 0.6297
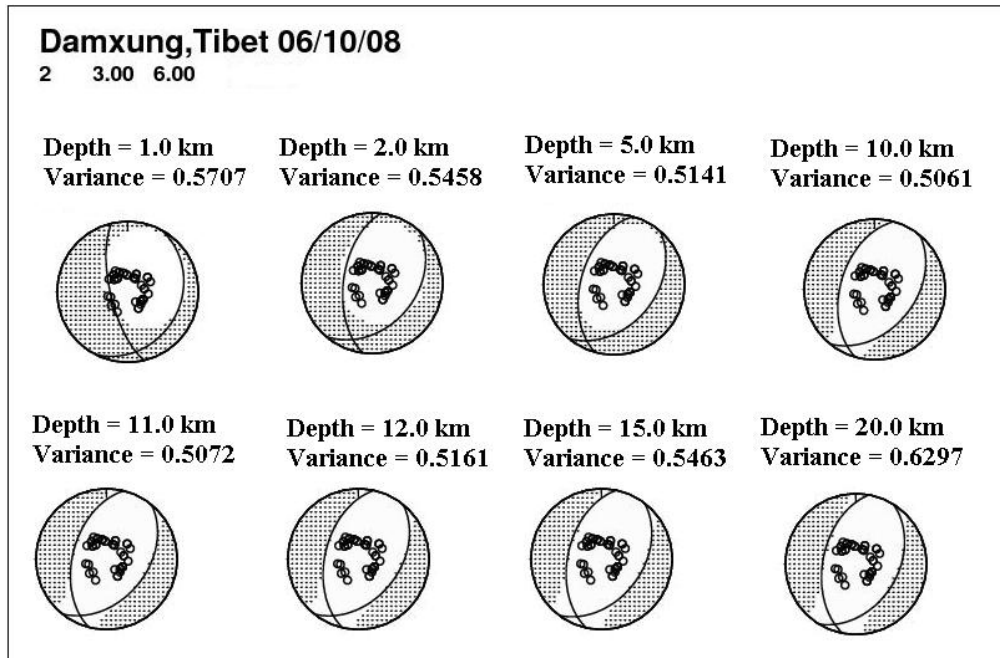
Figure 4.5c An example of focal mechanism for the 6 October 2008 Damxung earthquake with cosine-tapered ramp source time function and local velocity model. Depth and variance are shown on each solution.
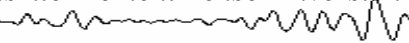
Table 4.5 Comparison of the focal mechanism solution for the 6 October 2008 Damxung mainshock with different source time function

M_0 ($*10^{18}$ mN)	M_W	Depth (km)	Strike (°)	Dip (°)	Rake (°)	Variance	Source time function
0.85	5.89	11.0	188.8	51.6	-114.2	0.4977	Triangular function
0.62	5.80	11.0	175.2	58.5	-133.8	0.5776	Impulse function
1.07	5.95	11.0	194.7	50.2	-105.9	0.5091	Trapezoid function
1.05	5.95	11.0	194.4	50.3	-106.4	0.5072	Cosine-tapered ramp function

4.3.4 Inversion results for 2008 Damxung earthquake

Although results represented in Table 4.5 are very similar, the first one of them is my preferred solution. The reason for selecting this solution is that it has the smallest variance or misfit between synthetic seismograms and observed waveforms. The source parameters are φ= 188.8°, δ = 51.6°, λ = - 114.2°, M_o = 0.85E+18 Nm, M_w =5.89 and the focal depth of approximately 11.0 km. It was in agreement with other reported solutions (Table 4.6). The result was obtained by 26-P and 14-SH waveforms with local crustal structure model near the source and a triangular source time function (Figure 4.6). The results indicate that the earthquake was dominated by normal fault with shallow depth.
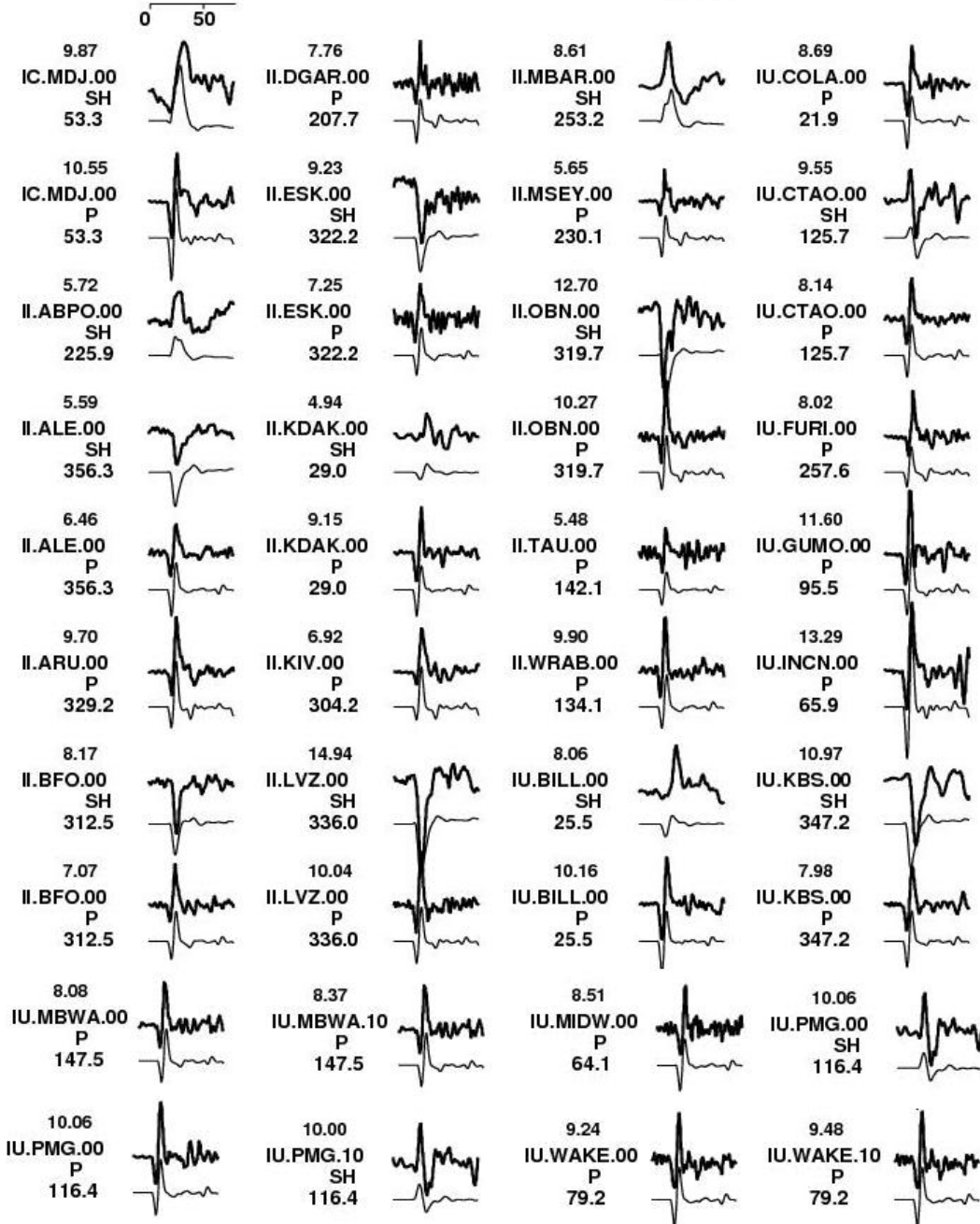
Table 4.6 Comparison of results with other reported results for the 2008 Damxung earthquake

Source	Strike (°)	Dip (°)	Slip (°)	Moment (10^{18}Nm)	Magnitude (M_w)	Depth (km)
GMCT	44/178	48/53	-55/-122	3.65	6.3	12.0
USGS	35/184	45/49	-67/-111	1.9	6.1	7.0
Gao *et al.* (2010)	38.9/183.3	46.4/49.5	-65/-115		6.2	9.6
This study	188.8	51.6	-114.2	0.85	5.89	11.0

Damxung, Tibet 06/10/08

3   3.00   6.00   0.4977

$M_0 = 0.85\ E{+}18\ Nm$ $M_w = 5.89$ $Depth = 11.0\ km$
$Strike = 188.8°$ $Dip = 51.6°$ $Rake = -114.2°$

9.87 IC.MDJ.00 SH 53.3	7.76 II.DGAR.00 P 207.7	8.61 II.MBAR.00 SH 253.2	8.69 IU.COLA.00 P 21.9
10.55 IC.MDJ.00 P 53.3	9.23 II.ESK.00 SH 322.2	5.65 II.MSEY.00 P 230.1	9.55 IU.CTAO.00 SH 125.7
5.72 II.ABPO.00 SH 225.9	7.25 II.ESK.00 P 322.2	12.70 II.OBN.00 SH 319.7	8.14 IU.CTAO.00 P 125.7
5.59 II.ALE.00 SH 356.3	4.94 II.KDAK.00 SH 29.0	10.27 II.OBN.00 P 319.7	8.02 IU.FURI.00 P 257.6
6.46 II.ALE.00 P 356.3	9.15 II.KDAK.00 P 29.0	5.48 II.TAU.00 P 142.1	11.60 IU.GUMO.00 P 95.5
9.70 II.ARU.00 P 329.2	6.92 II.KIV.00 P 304.2	9.90 II.WRAB.00 P 134.1	13.29 IU.INCN.00 P 65.9
8.17 II.BFO.00 SH 312.5	14.94 II.LVZ.00 SH 336.0	8.06 IU.BILL.00 SH 25.5	10.97 IU.KBS.00 SH 347.2
7.07 II.BFO.00 P 312.5	10.04 II.LVZ.00 P 336.0	10.16 IU.BILL.00 P 25.5	7.98 IU.KBS.00 P 347.2
8.08 IU.MBWA.00 P 147.5	8.37 IU.MBWA.10 P 147.5	8.51 IU.MIDW.00 P 64.1	10.06 IU.PMG.00 SH 116.4
10.06 IU.PMG.00 P 116.4	10.00 IU.PMG.10 SH 116.4	9.24 IU.WAKE.00 P 79.2	9.48 IU.WAKE.10 P 79.2

Figure 4.6 *The Top trace of each seismogram pair is the observed seismograms and the bottom trace is synthetic. The number above the station code and below the phase code indicates peak-to-peak amplitude in microns and the station azimuth, respectively. Source time function and focal mechanism is shown in the right corner and the middle of the page respectively, obtained by inversion of teleseismic 26-P and 14-SH waveforms with local velocity model (Table 4.4) for the 6 October 2008 Damxung mainshock.*

4.4 Inversion of the 1992 Nyimo earthquake

The results of the inversion of the 2008 Damxung earthquake suggest that the earthquake was dominated by normal slip type faulting with shallow depth. In order to further understand the characteristics of the focal mechanism surrounding this region, I chose another earthquake with moment magnitude 6.1 that occurred at Nyimo in 1992.

On 30 July 1992, an earthquake occurred in the Nyimo county, west of Lhasa, with epicenter approximately 94 km away from Lhasa; around 29 km away from the epicenter of the 2008 Damxung mainshock. The source parameters obtained from IRIS-DMC (http://www.iris.edu/dms/wilber.htm) are origin time, 08:24:46.6 (UTC), epicenter, 29.85°N, 90.16°E; depth, 14.10 km and M_w=6.1. The Global Centroid Moment Tensor (GCMT) solution for the 1992 Nyimo earthquake has a scalar moment $M_o = 1.79\times 10^{18}$ Nm , moment magnitude M_w =6.1, depth of 15.0 km, and double couple fault plane geometry of strike φ= 10°/196° and dip δ = 42°/49° with a rake λ = - 94°/ - 86° (http://www.globalcmt.org/CMTsearch.html). I performed a moment tensor inversion of this event in comparison to the 2008 Damxung event, using the appropriate local source structure.

4.4.1 Moment tensor inversion

The 3-component (BHZ, BHE,BHN) broadband teleseismic observations of the July 30, 1992 Nyimo earthquake used in the inversion were collected from 10 stations of GSN with Wilber II of IRIS (http://www.iris.edu/dms/wilber.htm) at teleseismic distances (30º < Δ < 90º). The stations coverage, location and parameters used in this inversion are shown in Figure 4.7, Table 4.7 and Table 4.8, respectively.
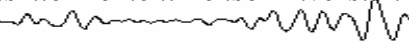
**Table 4.7** Location of stations used in the inversion of 1992 Nyimo event

Network	Station Code	Lat. (º)	Lon. (º)	Elevation (m)	Location
GSN - IRIS/USGS	COL	64.90	-147.79	320.00	College Outpost, Alaska, USA
GSN-IRIS/IDA	ERM	42.02	143.16	40.00	Erimo, Hokkaido Island, Japan
GSN - IRIS/USGS	GNI	40.15	44.74	1609.00	Garni, Armenia
GSN - IRIS/USGS	GUMO	13.59	144.87	170.00	Guam, Mariana Islands
GSN-IRIS/IDA	KIV	43.96	42.69	1210.00	Kislovodsk, Russia
GSN - IRIS/USGS	KONO	59.65	9.60	216.00	Kongsberg, Norway
GSN - IRIS/USGS	MAJO	36.55	138.20	405.00	Matsushiro, Japan
GSN-IRIS/IDA	OBN	55.11	36.57	160.00	Obninsk, Russia
GSN - IRIS/USGS	TOL	39.88	-4.05	480.00	Toledo, Spain
GSN - IRIS/USGS	YSS	46.96	142.76	150.00	Yuzhno Sakhalinsk, Russia

Table 4.8 Station parameters used in the inversion.

| Station Code	Distance (º)	Azimuth (º)	Back Azimuth (º)	Phase
COL	75.7	21.8	101.4	SH, P
ERM	44.1	58.7	-88.7	P
GNI	38.4	-61.5	91.5	P
GUMO	52.8	95.2	-63.0	P
KIV	40.1	-55.6	94.7	P, SH
KONO	60.3	-35.1	81.6	P, SH
MAJO	40.5	67.1	85.6	P
OBN	45.7	-40.1	101.4	P
TOL	74.7	-52.6	64.2	P, SH
YSS	43.9	51.5	-94.1	P,SH
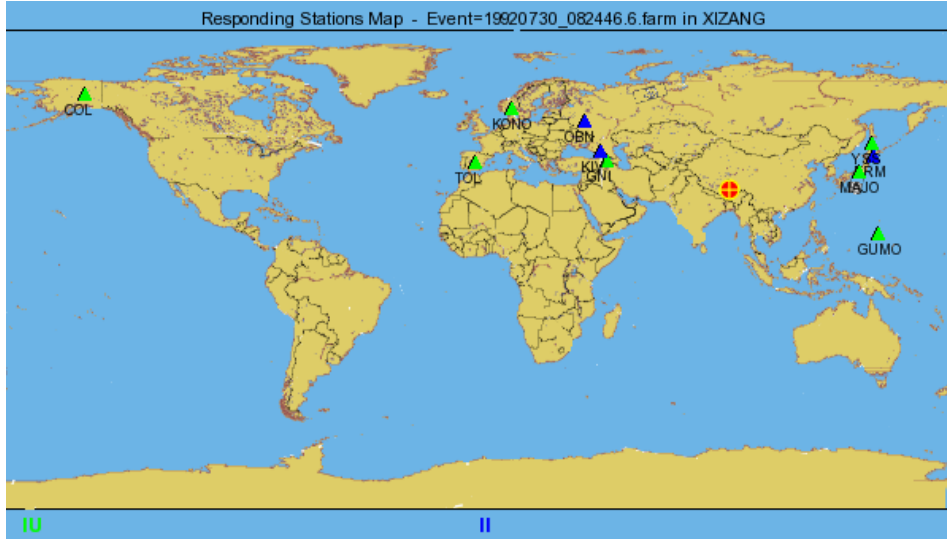
Figure 4.7 *Distribution of seismic stations used in the moment tensor inversion. Blue triangles represent the Global Seismograph Network (GSN - IRIS/IDA) and green triangles represent Global Seismograph Network (GSN - IRIS/USGS). The letters below the triangles indicate station code and the red circle indicates the epicenter of the July 30, 1992 Nyimo mainshock.*

Similarly as section 4.3, in order to obtain a precise depth, I tested several different *h* values as shown in Figure4.8. I found that the most accurate depth is about 10 km and the corresponding inversion result for 1992 Nyimo event is shown in Figure4.9.
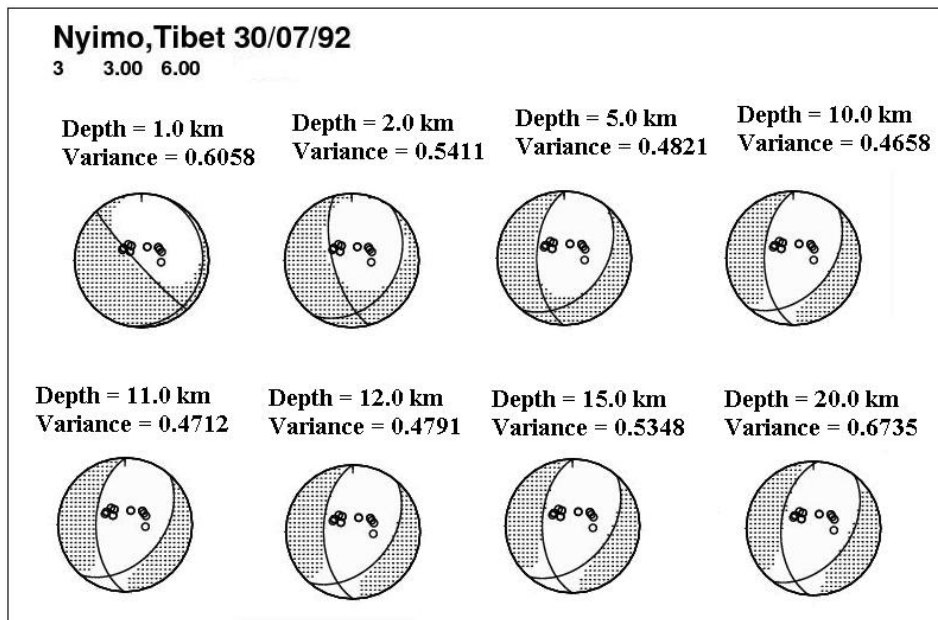
Figure4.8 *An example of focal mechanism for the 1992 Nyimo event with the triangular source time function and local velocity model. Depth and variance are shown on each solution.*
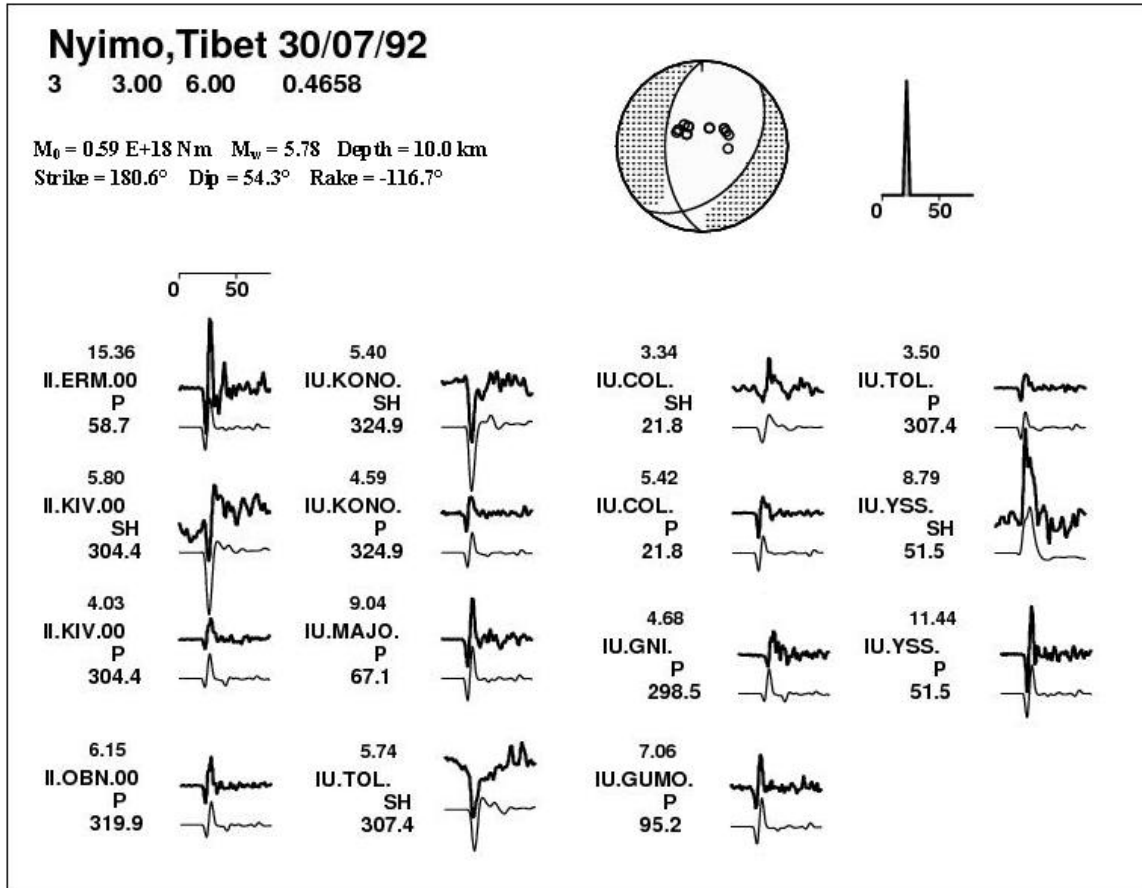
Figure4.9 *The top trace of each seismogram pair is the observed seismograms and the bottom trace is synthetic for the 30 July 1992 Nyimo mainshock. The number above the station code and below the phase code indicates peak-to-peak amplitude in microns and the station azimuth, respectively. Source time function of triangle and focal mechanism is display in the top right corner and the middle, respectively, base on teleseismic 10 P and 5 SH waveforms with local velocity structure..*

Figures 4.10a-4.10c show the seismograms of the 2008 Damxung event (M_w6.3) and 1992 Nyimo event (M_w6.1) recorded with the Global Seismographic Network (GSN) at teleseismic distance, station OBN. Traces are filtered using a passband 0.01 to 0.1 Hz.

The appearance of seismograms is very distance dependent and partly also dependent on the magnitude of the events (Havskov and Ottemöller, 2010). Obviously, the two traces of each box as shown in Figures 4.10a-4.10c are very similar, and the P-wave, S-wave and surface wave are very clear. But the 2008 Damxung event produce larger amplitudes than the 1992 Nyimo event, it mainly results from different seismic

magnitude because of the similar distance. Both events involved roughly normal slip faulting, having similar focal mechanisms, seismic moment and hypcentral depth.
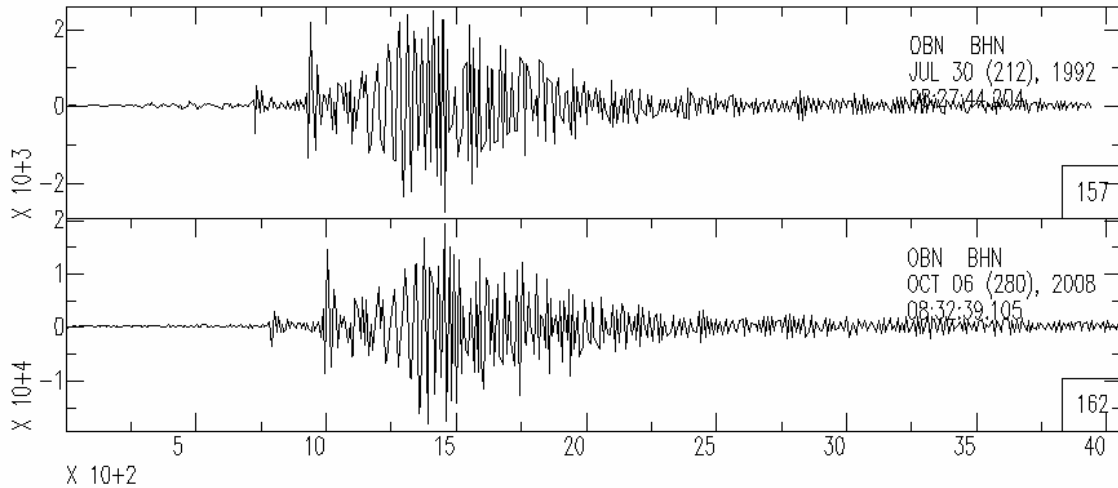
Figure 4.10a *Comparison of the NS-component seismogram of the 1992 Nyimo earthquake (top) and the NS-component seismogram of the 2008 Damxung earthquake (bottom) recorded by the Global Seismographic Network (GSN), station OBN.*
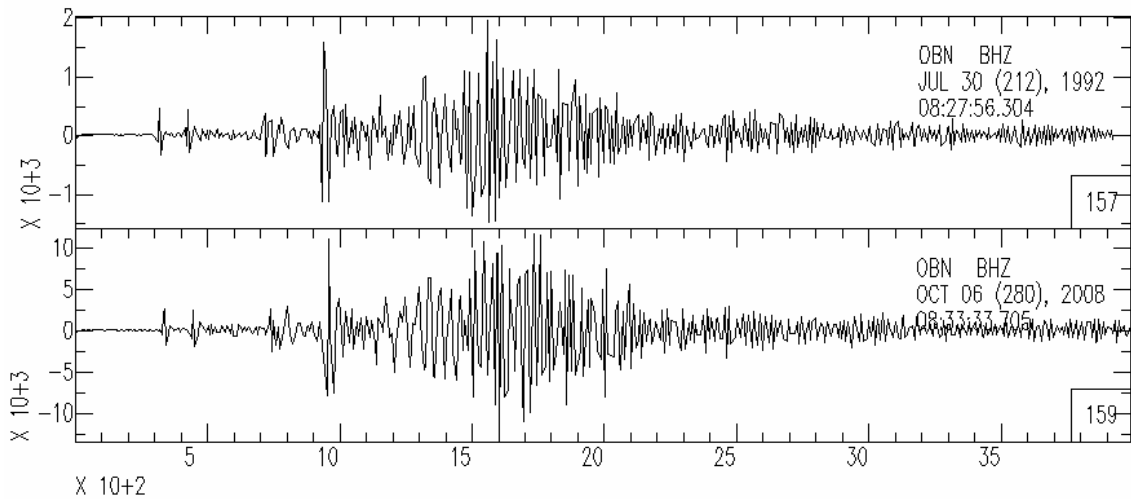
Figure 4.10b *Comparison of the vertical-component seismogram of the 1992 Nyimo earthquake (top) and the vertical component seismogram of the 2008 Damxung earthquake (bottom) recorded by the Global Seismographic Network (GSN), station OBN.*
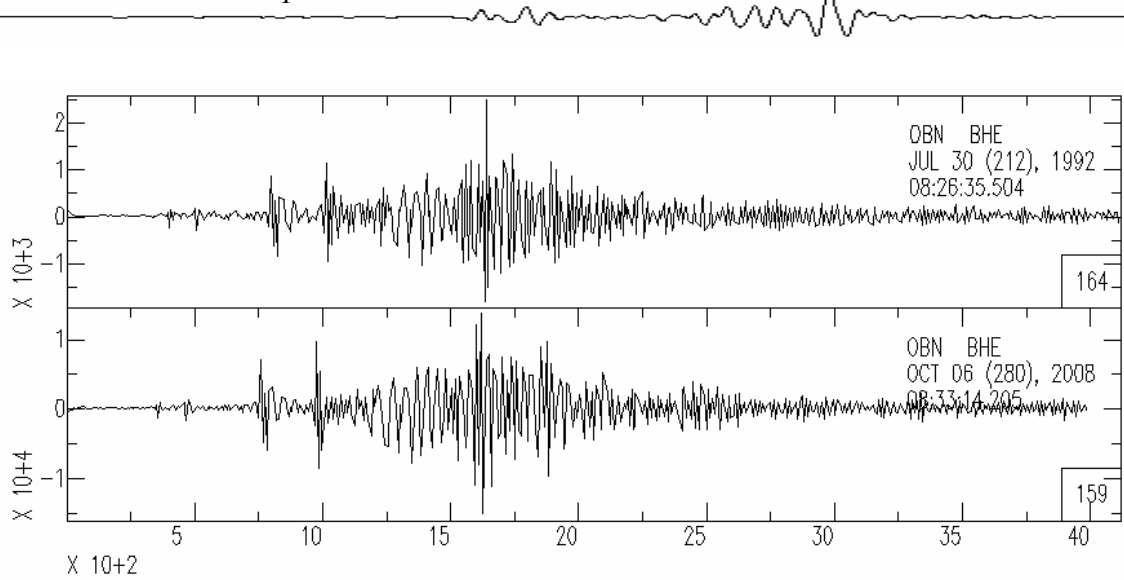
Figure 4.10c *Comparison of the EW-component seismogram of the 1992 Nyimo earthquake (top) and the EW- component seismogram of the 2008 Damxung earthquake (bottom) recorded by the Global Seismographic Network (GSN), station OBN.*

4.4.2 Inversion results for 1992 Nyimo earthquake

The results implied that the earthquake was also characterised by normal slip faulting with shallow depth. The best fit fault plane solution (Figure4.9) was φ= 180.6°, δ = 54.3°, λ = - 116.7°, M_o = 0.59E+18 Nm, M_w =5.78 and the focal depth of 10.0 km, based on 10-P and 5-SH waveforms with local crustal structure model near the source and a triangle source time function. The obtained focal mechanism solution was compared with GCMT solution as shown in Table 4.9. The result is similar to the result of the GCMT solution.

Table 4.9 Comparison of results with other reported results for the 1992 Nyimo earthquake

Source	Strike (°)	Dip (°)	Slip (°)	Moment (10^{18}Nm)	Magnitude (M_w)	Depth (km)
GMCT	10/196	42/49	-94/-86	1.79	6.1	15.0
This study	180.6	54.3	-116.7	0.59	5.78	10.0

43

Chapter **5**

Simulation of Ground Motion Using the Stochastic Finite Fault Method

The stochastic finite-fault methodology has been applied to model the acceleration time series near the rupture of large earthquakes for obtaining ground motion at the frequency of interest to earthquake engineers. This simulation technique has been widely used in the prediction of strong ground motions (Hanks and Mcguire, 1981; Boore, 1983, 1996; Boore and Atkinson, 1987; Beresnev and Atkinson, 1997, 1998a, 1998b; Ou and Herrmann, 1990; Shoja-Taheri and Ghofrani, 2007; Roumelioti and Beresnev, 2003; Motazedian and Atkinson, 2005; Motazedian and Moinfar, 2006).

In this chapter, the stochastic finite-fault method based on dynamic corner frequency proposed by Motazedian and Atkinson (2005) with the program EXSIM (Motazedian, 2009) is used to simulate the ground motion at the LSA station for the 2008 Damxung mainshock, using the seismic moment and orientation from the moment tensor inversion as input.

5.1 Simulation method and modeling parameters

In this simulation method by Motazedian and Atkinson (2005), a large fault is separated into a number of small subfaults. The ground motions contributed by each subfault can be computed by using stochastic point-source method. The ground motions of subfaults are summed with a proper time delay to obtain the ground motion acceleration from the entire fault as

$$a\left(t\right) = \sum_{i=1}^{nl} \sum_{j=1}^{nw} a_{ij}\left(t + \Delta t_{ij}\right) \qquad (5.1)$$

where *nl* and *nw* are the number of subfaults along the strike and dip of main fault, respectively, and Δt_{ij} is the relative delay time for the radiated wave from the *ij*th subfault

to reach the observation point. The $a_{ij}(t)$ is the acceleration of the *ij*th subfault at the observation point, calculated by the stochastic point-source method (Boore, 1983; Motazedian and Atkinson, 2005).

Based on the model by Motazedian and Atkinson (2005), the dynamic corner frequency of the *ij*th subfault, $f_{0ij}(t)$, are given by

$$f_{0ij} = \frac{4.9 \times 10^6 \beta}{N(t)^{\frac{1}{3}}} \left(\frac{\Delta\sigma}{M_{0ave}} \right)^{\frac{1}{3}} \tag{5.2}$$

where $M_{0ave} = M_0/N$ is the average seismic moment of subfaults in dyne-cm, in which M_0 is the seismic moment of the entire fault, N is the total number of subfaults ; $\Delta\sigma$ is the stress drop in bars, N(t) is the cumulative number of ruptured subfaults at time t, and β is a shear-wave velocity of the focal region in kilometers per second.

For $t = t_{end}$, the number of ruptured subfaults, $N_R(t = t_{end}) = N$. The corner frequency at the end of rupture is rewritten by

$$f_{0ij}\left(t_{end}\right) = 4.9 \times 10^6 \beta \left(\frac{\Delta\sigma}{M_0} \right)^{\frac{1}{3}} \tag{5.3}$$

when $t = t_{end}$, $f_{0ij}(t_{end}) = f_0$ which is the corner frequency of the entire fault.
And the acceleration spectrum of the *ij*th subfault, $A_{ij}(f)$, can be expressed as follows

$$A_{ij}(f) = \frac{CM_{0ij}H_{ij}(2\pi f)^2}{1 + \left(\frac{f}{f_{0ij}} \right)^2} \tag{5.4}$$

Where H_{ij} is a scaling factor that we apply to conserve the high-frequency spectral level of subfaults (Motazedian and Atkinson, 2005) and C is a constant (see Boore, 1983; Motazedian and Atkinson, 2005, for more details).

The modeling parameters used for the simulations of the Damxung earthquake are given in Table 5.2.

Based on the results of the moment tensor inversion in chapter 4 of this paper, the fault orientation (strike/dip), moments magnitude, and depth of the mainshock were 188.8º / 51.6º, 5.89 Mw and 11.0 km, respectively. Location of the epicenter at 29.66°N, 90.50°E was obtained from the Global Centroid Moment Tensor (GCMT). The fault dimension is 15 km×14 km adopted by Qiao *et al.* (2010) for the 2008 Damxung earthquake. Hence, the fault plane can be divided into 15 × 14 subfaults, and the size of each subfault is 1 km × 1 km.

According to Beresnev and Atkinson (1998b), the ratio of rupture velocity to shear-wave velocity is assumed to be 0.8. Because I did not found an available value of stress drop for this earthquake, I tested several different values of stress drop as shown in Figure 5.3c. I found that the best fit between simulated and observed acceleration response spectra is at around 60 bars. The shear-wave velocity and crustal density of the Tibetan Plateau averaged over the top 55 km are 3.6 km/s (Table 4.4) and 2.85 g/cm3, obtained from Table 4.4 and Xing et al. (2007). The attenuation and the propagation path effects are modeled by using the empirical attenuation, Q, geometric spreading and distance-dependent duration functions, as well as the kappa model (Beresnev and Atkinson, 1999; Yalcinkaya, 2005).

Q is quality factor, which is frequency dependent of the form

$$Q(f) = Q_0 f^{\eta} \qquad (5.5)$$

where Q_0 is the value of Q at 1 Hz, and η is the power-law frequency dependence (Fan and Lay, 2003; Xie, 2002). There are several studies of Lg attenuation in the Tibetan Plateau as listed in Table 5.1.

Table 5.1 Lg attenuation in the Tibetan Plateau

Location	Q_0	η	Frequency	Reference
Profile II	141±17	0.15±0.11	0.2-0.5Hz	(Fan and Lay, 2002)
	224±10	0.56±0.06	0.2-1.0 Hz	
Profile III	122±20	-0.19±0.15	0.2-0.5Hz	
	195±14	0.24±0.08	0.2-1.0 Hz	
Western portion of eastern Tibet	83±19	-0.07±0.19	0.2-0.5Hz	(Fan and Lay, 2003)
	108±5	0.19±0.06	0.2-1.0 Hz	
South-central Tibet	103±4	0.02±0.15	0.2-0.5Hz	
	187±5	0.57±0.05	0.2-1.0 Hz	
Eastern Tibet	126±9	0.37±0.02	0.2-3.6 Hz	(Xie, 2002)
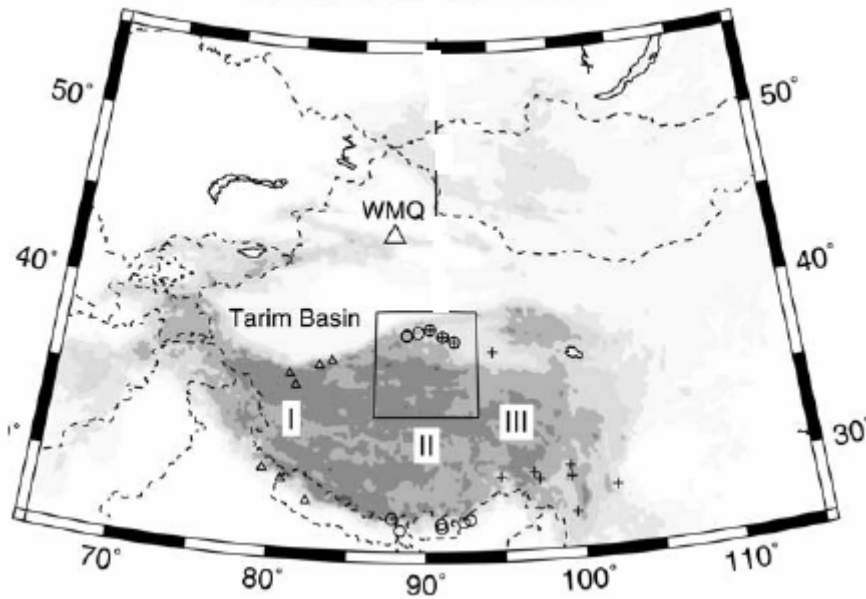
Figure 5.1 *A map showing locations of profiles II and III used for the Lg attenuation study in the Tibetan Plateau (Figure from (Fan and Lay, 2002))*

Based on Table 5.1, I tried several different values of the attenuation as shown in Figure 5.3b. I found that $Q_0 = 126$ and $\eta=0.37$ was most appropriate. Unfortunately, I have not found a value of near surface attenuation, kappa, which controls the path-independent high frequency decay of the spectrum (Anderson and Hough, 1984), in my study area. I assume it to be 0.04 s, which is an average value of the Wenchuan epicenter,

southern China by Ghasemi *et al.* (2010). In order to obtain more accurate results, I also tried several different kappa values as shown in Figure 5.3a, and believe that the k = 0.04 was more suitable. Distance-dependent duration was assumed as 0 (R < 10 km), 0.16R (10<R<70 km), -0.03R (70<R<130 km), 0.04R (R>130 km) (Beresnev and Atkinson, 1997; Beresnev and Atkinson, 1999; Yalcinkaya, 2005).

''The most obvious effect causing seismic wave amplitudes to vary with distance is geometric spreading '' (Stein and Wysession, 2003). The geometrical spreading function $G(r)$ was assumed to be in the following form (Beresnev and Atkinson, 1997; Beresnev and Atkinson, 1999; Motazedian and Atkinson, 2005):

$$G(r) = \begin{cases} 1/R & (R \leq 70\,km) \\ 1/R^0 & (70 < R \leq 130\,km) \\ (R)^{-0.5} & (R > 130\,km) \end{cases} \qquad (5.6)$$

Table 5.2 Modeling Parameters for Stochastic Finite-Fault with EXSIM

| Parameter	Parameter Value
Fault orientation (strike , dip)	188.8°/51.6°
Fault dimensions along strike and dip (km)	15 by 14
Subfault length and width (km)	1 by 1
Depth of the hypocenter (km)	11.0
Latitude and longitude of upper edge of fault	29.66°N, 90.50°E
Moment magnitude (M*w*)	5.89
Q(*f*)	$126f^{0.37}$
Distance-dependent duration	0 (R < 10 km), 0.16R(10<R<70 km), -0.03R (70<R<130 km), 0.04R (R>130 km)
Kappa (s)	0.04
Crustal shear-wave velocity (krn/s)	3.6
Crustal density (g/cm^3)	2.85
Geometric spreading	1/R (R $\leqslant$ 70 km) , 1/R^0 (70 $<$ R $\leqslant$ 130 km) 1/R$^{0.5}$ (R $>$ 130 km)
Stress parameter (bars)	60
Pulsing percentage	50%
Windowing function	Saragoni-Hart
Crustal amplification	Boore-Joyner (1997) western North America generic rock site
Rupture velocity /shear-wave velocity	0.8
Fault-slip distribution	unity slip for all subfaults

5.2 Ground-motion data

The Damxung earthquake was recorded at the LSA station, which has an epicentral distance around 75 km, and is operated by the IC (seismic network code of the New China Digital Seismograph Network). The station LSA is located on the southern edge of the Tibetan Plateau north of the Indus-Tsangpo suture (ITS) zone (Reese *et al.*, 1999). The ground motion data for comparison was taken from the three-component Global Seismographic Network (GSN) broadband stations of IRIS-DMC. The location of the station is shown in Figure 5.2 and its summary information is given in Table 5.3.

Unfortunately, in this simulation study I have only had one available station, since there is only one global seismic station in Tibet. Local seismic station data are more difficult to obtain.
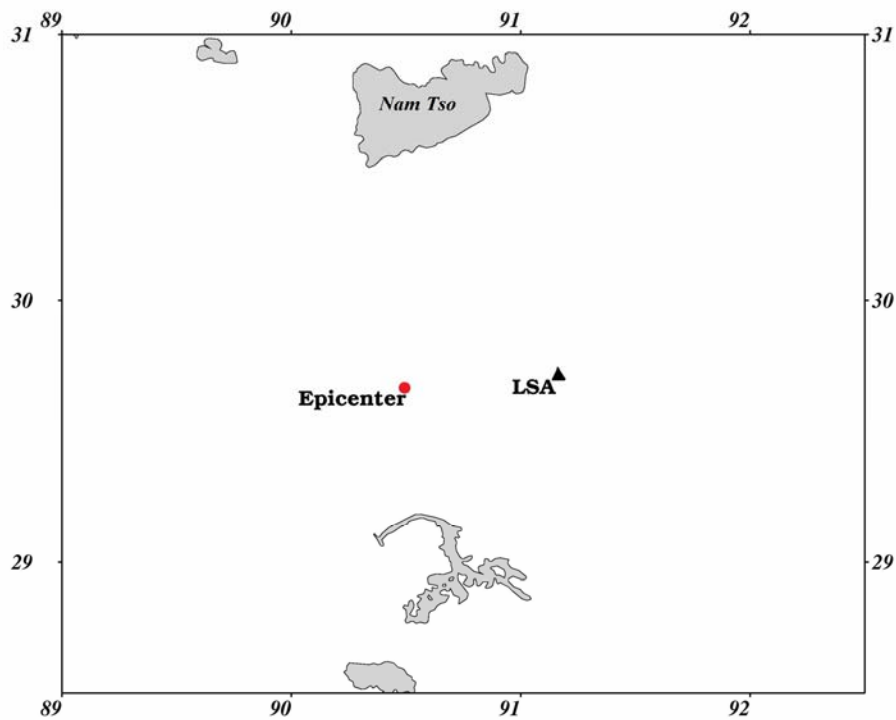
Figure 5.2 *A Map of the recording station used in this simulation. The black triangle represent the recording station and the red circle indicates the epicenter of the 6 October, 2008 Damxung mainshock.*
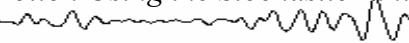
Table 5.3 Recording Station used in the stochastic finite fault simulation

Stadion Code	Latitude (º)	Longitude (º)	Elevation (m)	Fault Distance (km)	Location	Agency
LSA	29.70	91.13	3660.0	75.0	Lhasa, Tibet	IC*

* IC: New China Digital Seismograph Network

5.3 Data processing

5.3.1 Acceleration time series

Based on the modeling parameters (Table 5.2) and using the program EXSIM (Motazedian, 2009) for dynamic corner frequency I obtained the simulated acceleration time series as shown in Figure 5.4a, the top trace.

The ground motion data, which had been taken from GSN broadband stations of IRIS-DMC, converted to sac format with software, *rdseed.* The sac data was processed in SAC as following approaches in box, obtained the observed acceleration time series, which is saved in file.SAC.

```
SAC > xlim 200 600
SAC > r  2008.280.08.25.57.3102.IC.LSA.10.BHZ.R.SAC
SAC > rmean
SAC > rtr
SAC > hp c .1 p 2
SAC > transfer from polezero subtype SAC_PZs_IC_LSA_BHZ_00_1999.209.00.00.00.0000_2010.292.24.60.60.99999 freq 0. .01
SAC > dif
SAC > dif
SAC > p
SAC > w  file.SAC
```

Then the data placed in file.SAC converted to *ASCII* format with the command in SAC: *conv from SAC file.SAC to alpha newfile*. Finally, the observed acceleration time series was obtained as shown in Figure 5.4a.

5.3.2 Acceleration response spectra

The acceleration response spectra were obtained with the algorithm, called *response.* According to the modeling parameter in Table 5.2, and in order to obtain more accurate

simulation, I tested to change the parameter values, for example, using different kappa, Q-value, stress drop and active pulsing area for more detail in following.

By using a typical value of stress drop of 50 bars, keeping other parameters (Table 5.2) simulations were performed for different kappa values of 0.001, 0.005, 0.01, 0.04, 0.1 and 0.5 , and I obtained the response spectra as shown in Figure 5.2.3 a. I have found the value of zero-distance attenuation (kappa) is controlling the level of low frequency in acceleration response spectra more than high frequency.

Assuming the stress drop of 50 bars, all the other parameters have been kept as in Table 5.2, using different Q-value, including $Q_1=126 \ f^{0.37}$, $Q_{min}=1000$; $Q_2=126 \ f^{0.37}$, $Q_{min}=500$; $Q_3=224 \ f^{0.56}$, $Q_{min}=1000$; $Q_4=224 \ f^{0.56}$, $Q_{min}=500$; $Q_5=108 \ f^{0.19}$, $Q_{min}=1000$; $Q_6=108 f^{0.19}$, $Q_{min}=500$, got the response spectra as shown in Figure 5.3b.

Similarly, using different stress drop and active pulsing area obtained the response spectra as shown in Figure 5.3c and 5.3d.

5.4 Results of the simulation

I have tested several different values of modeling parameter, for example, using different stress drop, kappa, Q-value and active pulsing area, to simulate 2008 Damxung earthquake at LSA. The final input parameters were decided as shown in Table 5.2, based on Figure 5.3a, 5.3b, 5.3c and 5.3d and my results from chapter 4 as well as other articles. I have thought the Figure 5.4b is the satisfactory acceleration response spectra, in other words, there is good agreement between simulated and observed records. Figure 5.4a is the corresponding acceleration time series. The simulated peak ground acceleration (PGA) is 7.9595 cm/s^2. The observed PGA of E-W acceleration components, N-S acceleration components and vertical components are 13.3326 cm/s^2, 6.5009 cm/s^2 and 7.6334 cm/s^2, respectively.
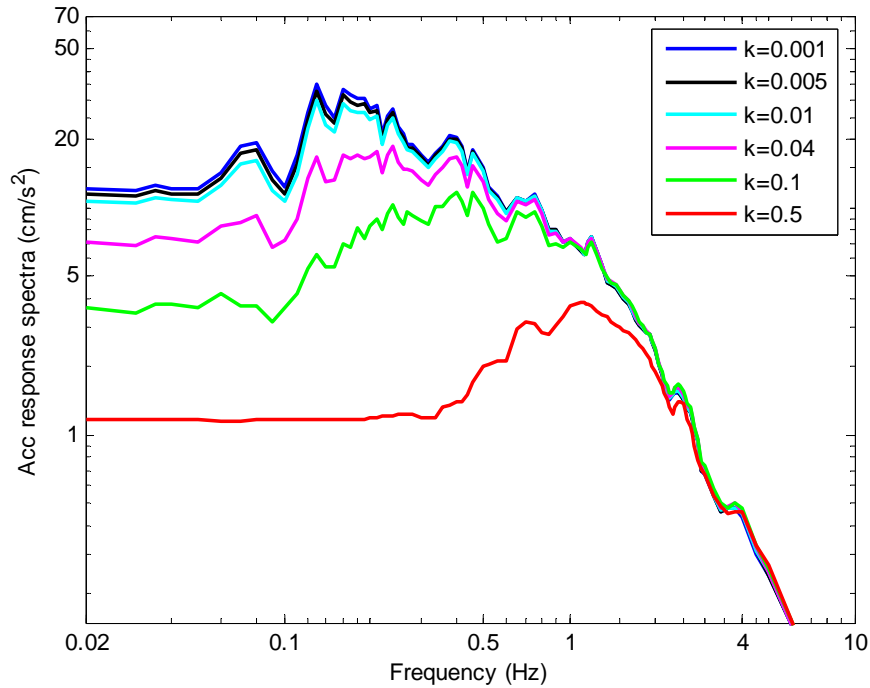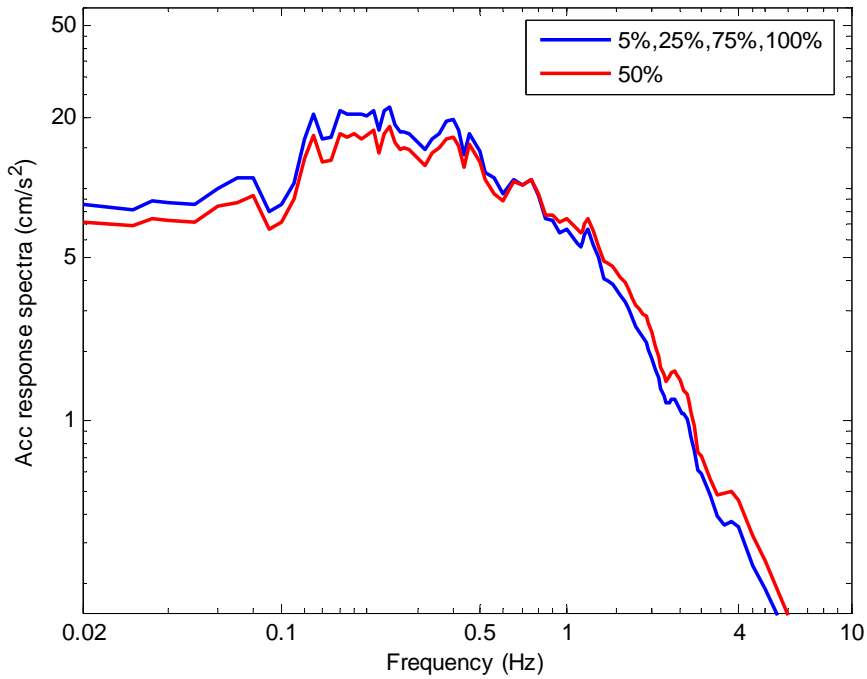
Figure 5.3a *Simulated acceleration response spectra for event $M_w5.89$ at LSA station for different kappa parameters. Assumed stress drop of 50 bars and all the other parameters have been kept in Table 5.2.*
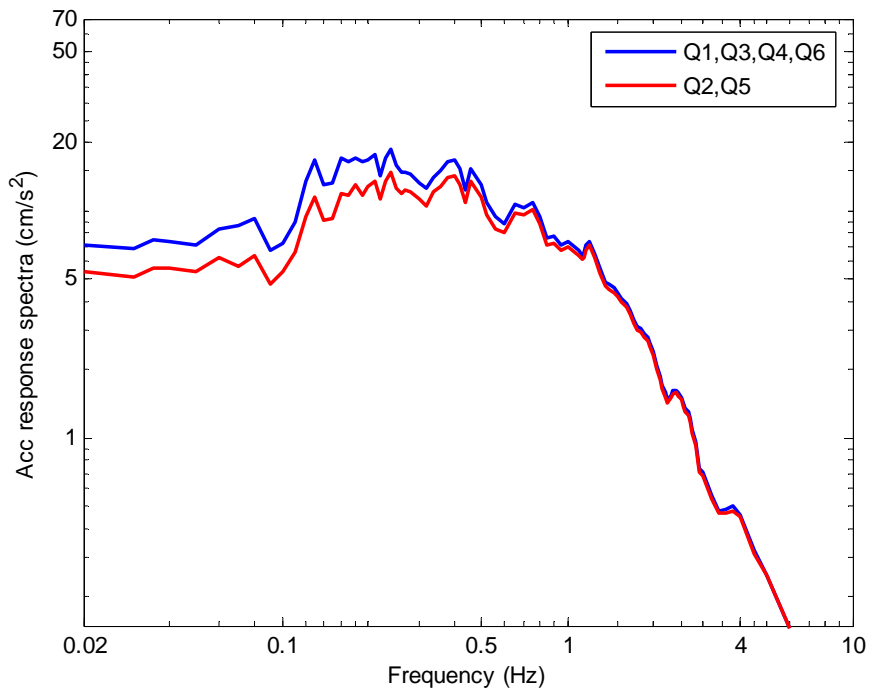
Figure 5.3b *Simulated acceleration response spectra for event $M_w5.89$ at LSA station for different attenuation parameters. Assumed stress drop of 50 bars and all the other parameters have been kept in Table 5.2. The meaning of each Q see section 5.3.2.*
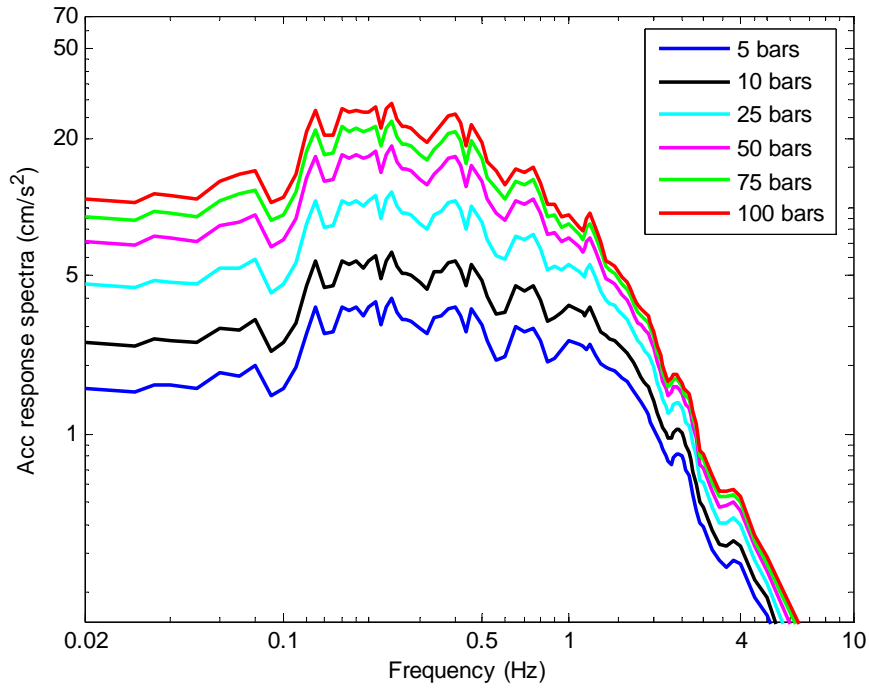
Figure 5.3c *Simulated acceleration response spectra for event $M_w5.89$ at LSA station for different stress parameters. All the other parameters have been kept in Table 5.2.*
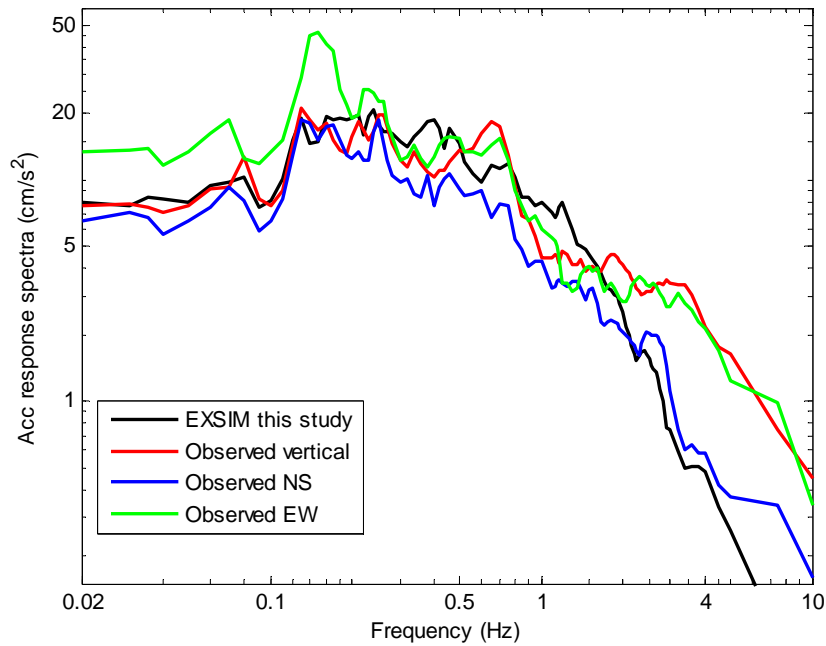

Figure 5.3d *Simulated acceleration response spectra for event $M_w5.89$ at LSA station for different active pulsing area. Assumed stress drop of 50 bars and all the other parameters have been kept in Table 5.2.*
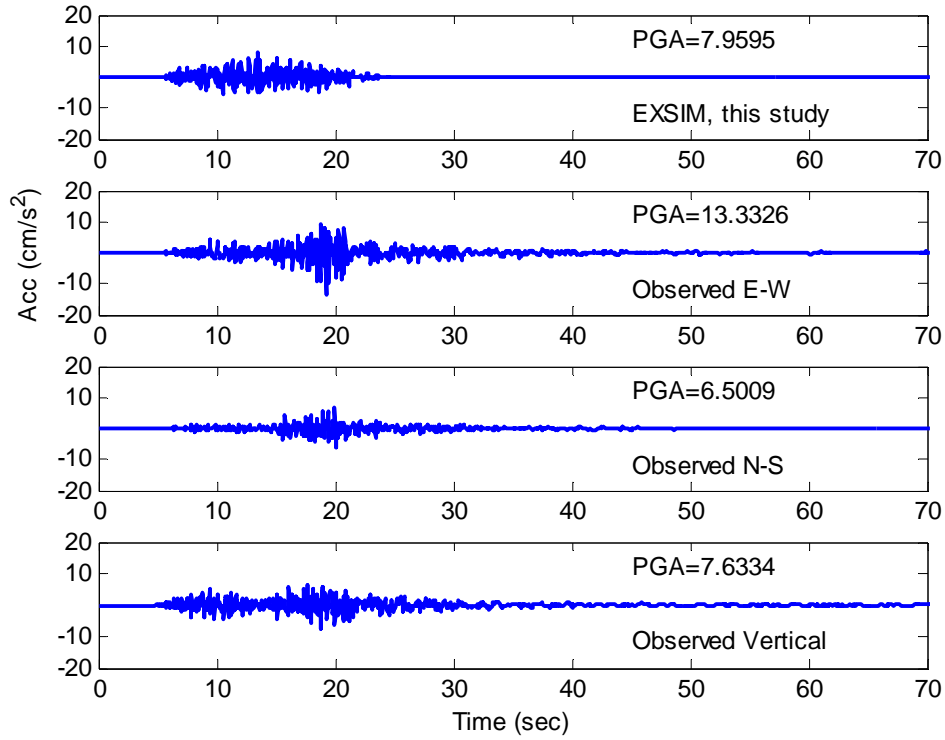
Figure 5.4a *Comparison between simulated with parameters Table 5.2 and observed (E-W, N-S and vertical components) acceleration time series for event $M_w5.89$ at LSA station. The peak ground acceleration in cm/s^2 is shown to the right corner of each box ,obtained with parameter in Table 5.2.*

Figure 5.4b *Acceleration response spectra for event $M_w5.89$ at LSA station with parameter in Table 5.2.*

Chapter **6**

Discussion

I have presented the outcome of inversion and simulation for the 2008 Damxung and 1992 Nyimo earthquakes. The results of this thesis are discussed below.

I used body-wave inversion method by Kikuchi and Kanamori with their algorithm (2003) and the broadband teleseismic seismograms recorded by Global Seismographic Network (GSN) to determine the focal mechanism, seismic moment and focal depth for 2008 Damxung and 1992 Nyimo earthquakes. The results of the moment tensor inversion as shown in Figures 4.6 and 4.9 suggest that both events were a normal slip type faulting at shallow depths with an approximate N-S trending.

In this work, I found that the choice of these three parameters which were the depth of the reference point, source time function and crustal structure model, were most important. Therefore, I tried to test a variety of the parameter settings in order to obtain a better result.

According to the published results of the focal depth of the 2008 Damxung earthquake, I varied the depth of the reference point (section 4.3) for calculation synthetic data from 1 km to 20 km by 1 km increments and other parameters were kept the same setting value to determine the appropriate depth, as shown in Figure 4.4. The obtained results indicated that the variance between synthetic and observed seismograms varied from case to case, but the appropriate depth is about 11 km. Thus, I decided to set the depth of the reference point to 11km for determination source parameters.

In addition, I used different source time functions, e.g., impulse source time function, trapezoid source time function, cosine-tapered ramp source function and angular source time function. Although they also had an impact on the results (Table 4.5), the result of the corresponding triangular source function (Figure 4.6) has the smallest variance or misfit between synthetic seismograms and recorded waveforms. Hence, the triangular source function was assumed for this inversion.

Finally, the fault plane solution of the 2008 Damxung event has been used for two different crustal structure models which were the J-B model (Table 4.3) and the local

earth model near the rupture (Table 4.4). Comparisons of the results are shown in Figure 4.2 and Figure 4.6. Obviously, the result in Figure 4.6 has the smallest variance and it was obtained by using local crustal velocity structure. Thus, I thought that the focal mechanism solution shown in Figure 4.6 was satisfactory results of the inversion for the 2008 Damxung event.

Comparing the solution of the 2008 Damxung earthquake (Figure 4.6) with the solution of the 1992 Nyimo earthquake (Figure4.9), I found that both events were normal faulting (Figure 6.1) and the source parameters are similar.
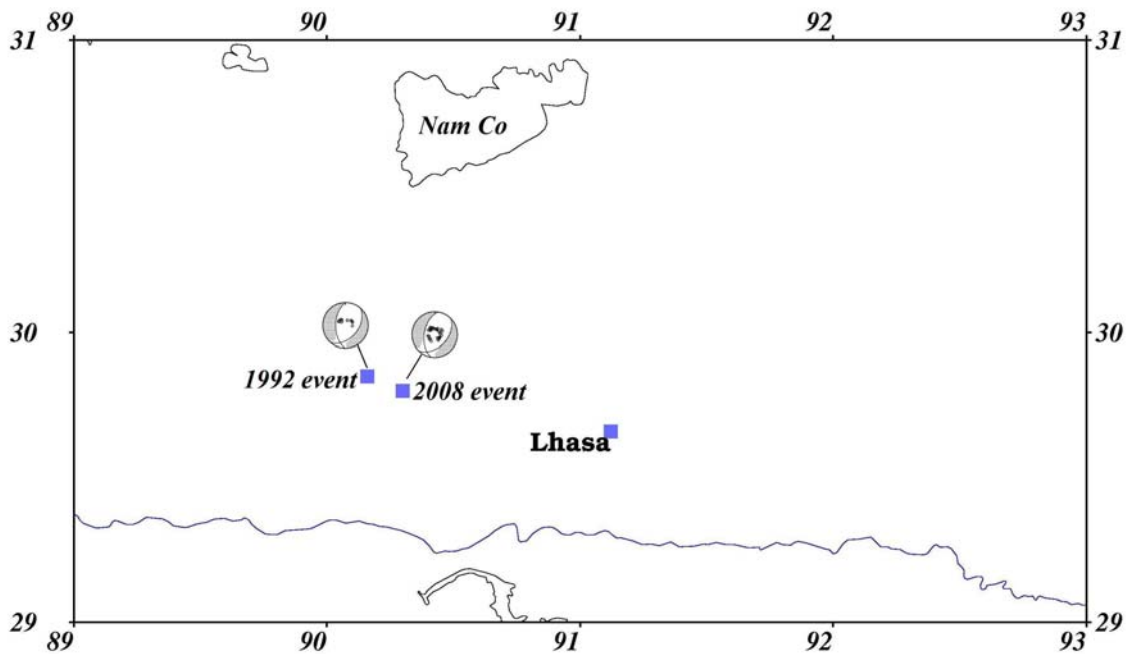
Figure 6.1 *Focal mechanisms for the 2008 Damxung and 1992 Nyimo earthquakes.*

In Tibet, because seismic stations are very sparse and data from existing local stations is difficult to obtain. I can only use teleseismic data to carry out this inversion study. I think that the results may be further refined with more precise input parameters and local data in future.

According to the strain-rate field of the Tibetan Plateau (Figure 6.4) by Gan *et al.* (2007), the largest compression and shortening is in the direction of India-Eurasia convergence on the southern Tibetan Plateau and Himalayan terrane. This is also shown in the stress map (Figure 6.3). The typical compression rate is about 30–60 nano-strain/yr [1], with some values as high as approximately 70 nano-strain/yr. while the compression rate along the convergence direction decreases remarkably to a level of about 15–20 nano-strain/yr for most of the places in Lhasa terrane. In the middle of the eastern part of the southern plateau between the longitudes of 86ºE and 92ºE, transverse extension is significant with typical values as large as about 15–25 nano-strain/yr. The stress vectors in Figure 6.3 for the Tibetan Plateau and adjacent regions and the focal mechanism solutions in Figure 6.2 show that the central part of the Tibetan Plateau is dominated by approximately N-S striking normal faults. This results are from transverse extension in this region.

GPS velocities further indicate that both within the central part of the Tibetan Plateau and along its borders, including the Himalaya, the Altyn Tagh and the Qilian Shan, are undergoing horizontal shortening as shown in Figure 6.2, where the colored numbers in represent respective velocity of crustal motion in mm/yr. Meantime the plateau is currently undergoing approximately east-west extension with velocity of 22±3 mm/yr *(Zhang et al., 2004).*

The stress pattern (Figure 6.3) shows that along the Himalayan margins, northwestern borders and eastern parts of the Tibetan Plateau are dominated by thrust faulting, while normal faults and strike-slip faults control the interior of the plateau. This is in agreement with the results from my focal mechanism solutions (Figure 2.5).

---

[1] A strain is a normalized measure of deformation representing the displacement between particles in the body relative to a reference length. In one dimensional case，strain = $\Delta l/l_0$, where l is the length under applied stress, l_0 is the original length and $\Delta l = l_0 - l$ (http://en.wikipedia.org/wiki/Strain_rate).
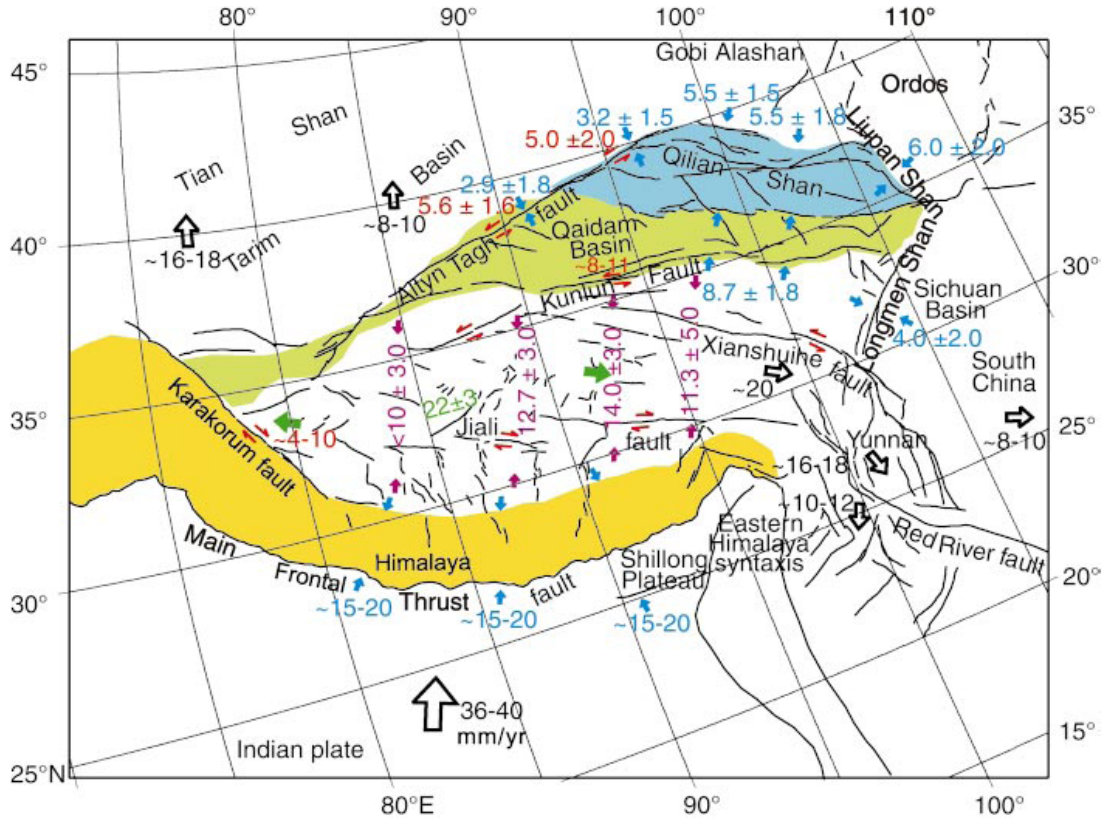
Figure 6.2 *Simplified tectonic map showing active faults and movements of Tibetan Plateau and its margins constrained by global positioning system measurements. Numbers are rates of movement (mm/yr). Bold purple arrows indicate N20ºE shortening across interior of plateau. Blue arrows indicate shortening perpendicular to margins of plateau. Green arrows indicate extension in western and central Tibet. Red arrows indicate strike-slip faulting. Open black arrows denote relative motion with respect to stable Eurasia. Colored numbers show respective amounts (Zhang, Shen al., 2004).*
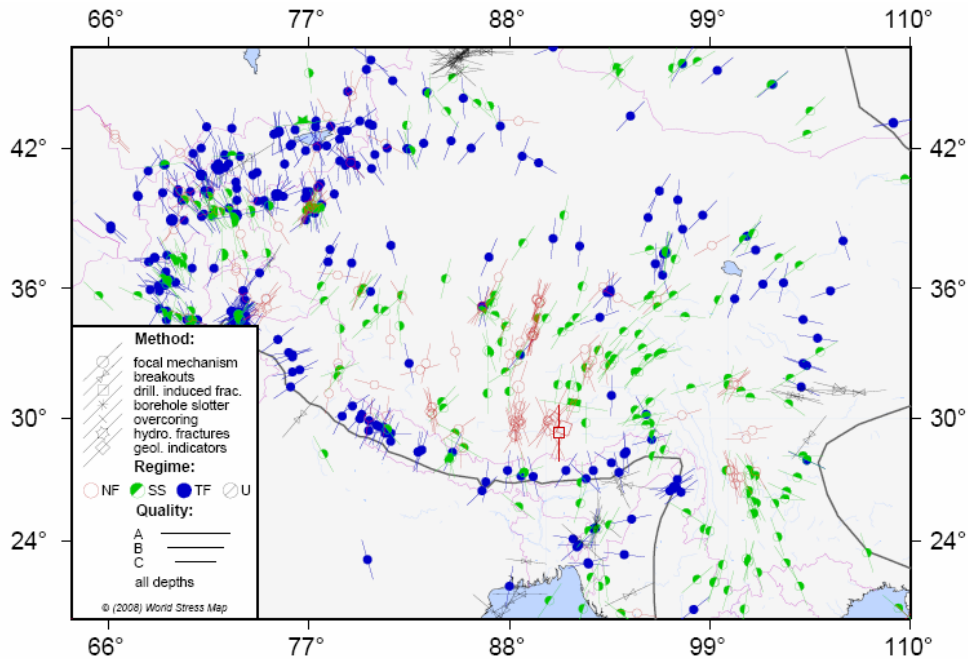
Figure 6.3 *Tectonics stress map in the Tibetan Plateau obtained from the World Stress Map (WSM) Project, available at http://dc-app3-14.gfz-potsdam.de/pub/casmo/casmo_frame.html. The red vectors represent normal faults; the blue vectors indicate thrust faults and the green vectors refer to strike-slip faults.*
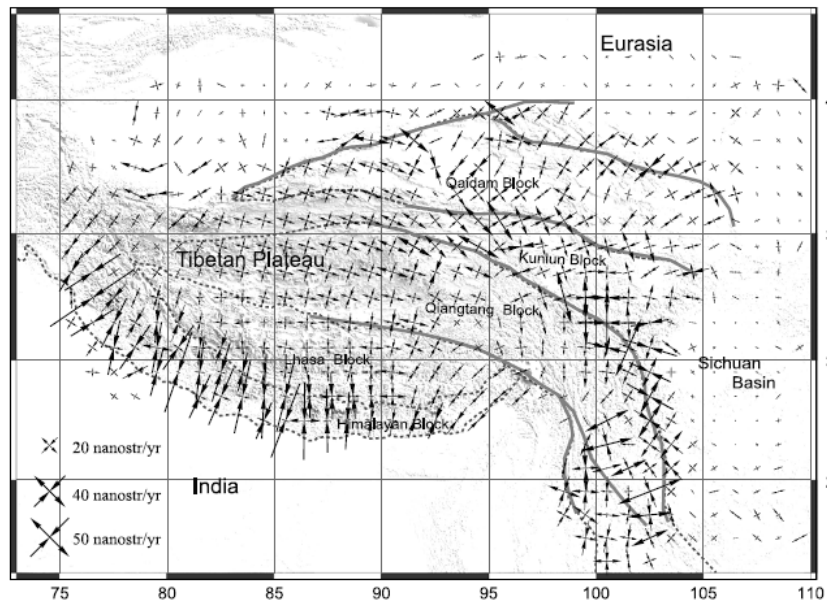

Figure 6.4 *Strain rate field of the Tibetan Plateau deduced from GPS velocities. The thick black solid lines indicate principal active faults. The dashed lines indicate the boundaries of tectonic blocks (Gan et al., 2007).*

In order to estimate how the simulated acceleration response spectra varies with frequency, I changed the stress drop, zero distance kappa factor, active pulsing area and Q-value, respectively, while other remaining parameters were kept in Table 5.2. Figures 5.3a-5.3d showed the corresponding response spectra.

Figures 5.3b and 5.3d indicate that the level of lower frequency of the acceleration response spectra, approximately below 1 Hz, was controlled by both the pulsing percentage of the active area and attenuation. While the parameters of both the zero distance kappa factors and the stress drop affected the level of the whole frequency range between 0.02 and 10 Hz, the impact on the level of lower frequency was still greater than higher frequency as shown in Figures 5.3a and 5.3c. While the detailed input parameters affecting the simulated result at a site are complicated.

Figures 6.5-6.7 show examples of acceleration response spectra with stress drop of 40, 50 and 70 bars respectively, and other parameters were kept as in Table 5.2. The most fitting results were shown in Figures 5.4a and 5.4b. Unfortunately, as mentioned above since there is no available seismic station near the fault rupture, and the simulated site, the LSA station is further away from the epicenter of 2008 Damxung event. For this reason, I consider that the accuracy of the simulated results probably is limited.
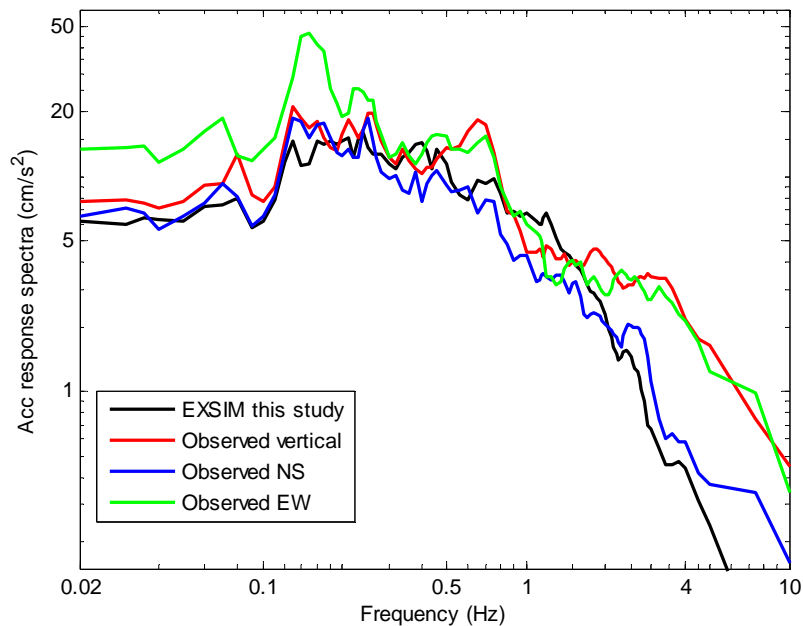
Figure 6.5 *Acceleration response spectra for event $M_w5.89$ at LSA station. Assumed the stress drop of 40 bars and all the other parameters have been kept in Table 5.2.*
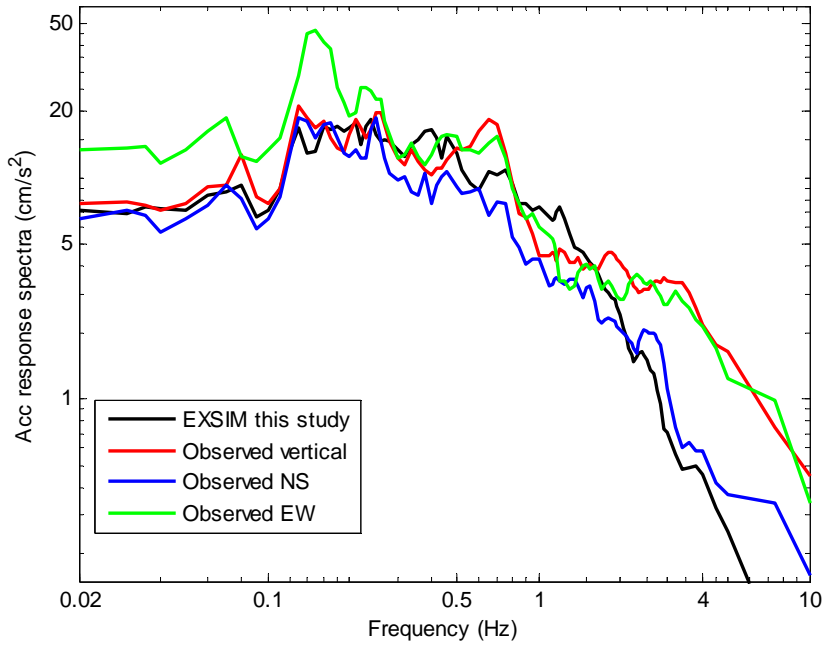
Figure 6.6 *Acceleration response spectra for event M_w5.89 at LSA station. Assumed the stress drop of 50 bars and all the other parameters have been kept in Table 5.2.*
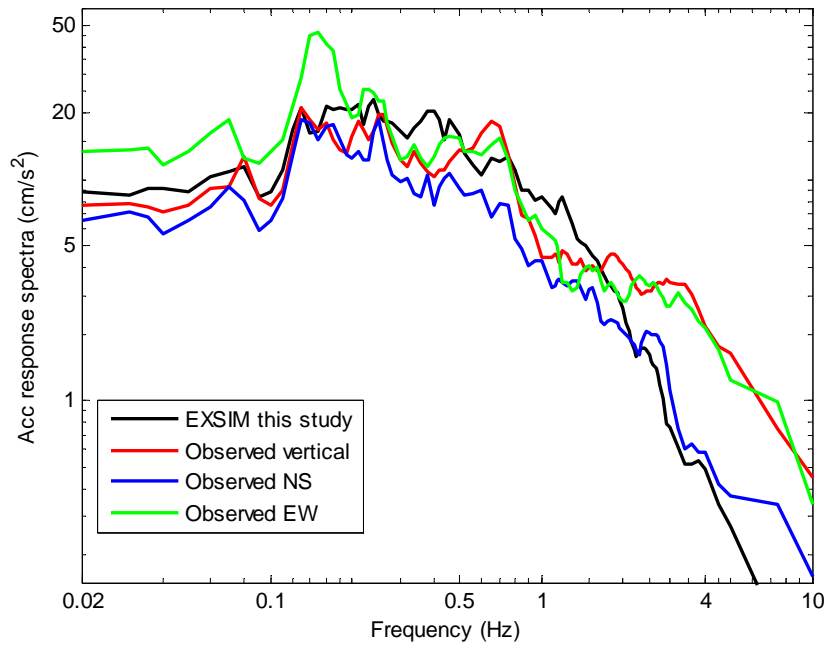
Figure 6.7 *Acceleration response spectra for event M_w5.89 at LSA station. Assumed the stress drop of 70 bars and all the other parameters have been kept in Table 5.2.*

Chapter 7

Conclusion

In this thesis I have briefly described the seismic-tectonics of the Tibetan Plateau and around Lhasa as well as introduced the basic situation of seismic station in Tibet. The major purpose of this study was twofold. The first was using the body-wave inversion method with the algorithm by Kikuchi and Kanamori (2003) to determine the source parameters for the 2008 Damxung and 1992 Nyimo events. The second was using the stochastic finite-fault simulation modeling technique based on dynamic corner frequency with the program EXSIM (Motazedian, 2009) to simulate the ground motion from the mainshock of the 2008 Damxung earthquake at LSA station. On the basis of the work of this thesis the following conclusions are made:

- The source parameters for the 2008 Damxung and 1992 Nyimo events were obtained by using body-wave inversion method with the broadband teleseismic seismograms at distance between 30° and 90° recorded by the Global Seismographic Network (GSN). I obtained synthetics that were in good agreement with observed seismograms. This study is necessary in order to improve the understanding of the local fault plane systems and seismo-tectonic processes and also to try to understand the causes of the earthquakes. A better focal mechanism solution was obtained with an appropriate velocity model at the source.

- Based on the input parameters (Table 5.2), acceleration time series (Figure 5.4a) and acceleration response spectra in the frequency band of 0.02 to 10 Hz (Figure 5.4b) were simulated. The simulation result overall agrees with the observed acceleration response spectra. The understanding of the stochastic finite fault technique for simulation acceleration is very beneficial for future studies in seismic hazard evaluations in data-deprived areas, such as Tibet.

References

Armijo, R., Tapponnier, P., Mercier, J. L., and Han, T. L. (1986). Quaternary extension in southern Tibet: field observation and tectonic implications. *Journal of geophysical research* 91, 13803–13872.

Barker, J. S., and Langston, C. A. (1981). Inversion of teleseismic body waves for the moment tensor of the 1978 Thessaloniki, Greece, Earthquake. *Bulletin of the Seismological Society of America* Vol. 71, No. 5, 1423-1444.

Barker, J. S., and Langston, C. A. (1983). A teleseismic body-wave analysis of the may 1980 Mammoth lakes, California, earthquakes. *Bulletin of the Seismological Society of America* 73 (2), 419-434.

Beresnev, I. A., and Atkinson, G. M. (1997). Modeling finite-fault radiation from the ω^n spectrum. *Bulletin of the Seismological Society of America* 87 (1), 67-84.

Beresnev, I. A., and Atkinson, G. M. (1998a). A FORTRAN program for simulating stochastic acceleration time histories from finite fault. *Seismol. Res. Lett.* 69, 27-32.

Beresnev, I. A., and Atkinson, G. M. (1998b). Stochastic finite-fault modeling of ground motion from the 1994 Northridge, California, earthquake. *Bulletin of the Seismological Society of America* 88 (6), 1392-1401.

Beresnev, I. A., and Atkinson, G. M. (1999). Generic finite-fault model for ground-motion prediction in eastern north America. *Bulletin of the Seismological Society of America* 89 (3), 608-625.

Boore, D. M. (1983). Stochastic simulation of high-frequancy ground motions based on seismological models of the radiated spectra. *Bulletin of the Seismological Society of America* 73 (6), 1865-1894.

Boore, D. M., and Atkinson, G. M. (1987). Stochastic prediction of ground motion and spectral response parameters at hard-rock sites in eastern north america. *Bulletin of the Seismological Society of America* 77 (2), 440-467.

Boore, D. M. (1996). SMSIM — fortran programs for simulating ground motions from earthquakes. *U. S. Geoological Survey* Version 2.0- A Revision of OFR 96-80-A, 1-56.

Boore, D. M., and Joyner, W. B. (1997). site amplification for generic rock sites. *Bulletin of the Seismological Society of America* 87 (2), 327-341.

Burdick, L. J., and Mellman, G. R. (1976). Inversion of the body waves from the Borrego mountain earthquake to the source mechanism. *Bulletin of the Seismological Society of America* 66,No.5, 1485-1499.

Castro, R. R., and Ruı́z-Cruz, E. (2005). Stochastic modeling of the 30 September 1999 Mw 7.5 earthquake,Oaxaca, Mexico. *Bulletin of the Seismological Society of America* 95 (6), 2259-2271.

Chen, Q. Z., Freymueller, J. T., Wang, Q., Yang, Z. Q., Xu, C. J., and Liu, C. (2004). A deforming block model for the present-day tectonics of Tibet. *J. of Geophys. Res.* 109,

Ciren. (2006). Local seismicity and seismic hazard around Lhsa, Tibet. Master thesis.

Cogan, M. J., Nelson, K. D., Kidd, W. S. F., Wu, C., and Team, P. I. (1998). Shallow structure of the Yadong-Gulu rift, southern Tibet, from refraction analysis of Project INDEPTH common midpoint data. *Tectonics* 17(1), 46-61.

Cui-Ping, Z., Zhang-Li, C., si-Hua, Z., and Zhi-Qiang, Z. (2008). Moment inversion of moderate earthquakes and the locally perturbed stress field in the Jiashi source region (in Chinese). *Chinese Journal of Geophysics* 51 (3), 782-792.

Deng, Q. D., Zhang, P. Z., Ran, Y. K., Yang, X. P., Min, W., and Chu, Q. Z. (2003). Basic characteristics of active tectonics of China. *Sience in China* 46 (4),

Dewey, J. F., Shacketon, R. M., Chengfa, C., and Yiyin, S. (1988). The tectonic evolution of the Tibet plateau. *Phil. Trans. R. Soc. Lond. A* 327, 327-413.

Estabrook, C. H. (1999). Body wave inversion of the 1970 and 1963 South American large deep-focus earthquakes. *J. of Geophys. Res.* 104 (B12), 28751-28767.

Fan, G. W., and Lay, T. (2002). Characteristics of Lg attenuation in the Tibetan Plateau. *J. of Geophys. Res.* 107 (B10).

Fan, G. W., and Lay, T. (2003). Strong Lg attenuation in the Tibetan Plateau. *Bulletin of the Seismological Society of America* 93 (5), 2264-2272.

Fielding, E., Isacks, B., Barazang, M., and Duacan, C. (1994). How flat is Tibet? 22, 163-167.

Gan, W., Zhang, P. Z., Shen, Z. K., Niu, Z. J., Wan, M., Wan, Y. G., Zhou, D. M., and Cheng, J. (2007). Present-day crustal motion within the Tibetan Plateau inferred from GPS measurements. *J. of Geophys. Res.* 112.

Gao, X., Duan, Z. Q., Wang, W. M., and Gao, Z. (2010). Rupture process of the Oct. 6, 2008 Ms 6.6 Damxung earthquake, Tibet, China (in chinese). *Chinese Journal of Geophysics* 53 (9).

Ghasemi, H., Fukushima, Y., Koketsu, K., Miyake, H., Wang, Z., and Anderson, J. G. (2010). Ground-motion simulation for the 2008 Wenchuan,China, earthquake using the stochastic finite-fault method. *Bulletin of the Seismological Society of America* 100 (5B), 2476-2490.

Haines, S. S., Klemperer, S. L., Brown, L., Jingru, G., Mechie, J., Meissner, R., Ross, A., and Wenjin, Z. (2003). INDEPTH III seismic data: From surface observations to deep crustal processes in Tibet. *TECTONICS* 22 (1), 1-18.

Hanks, T. C., and Mcguire, R. K. (1981). The character of high-frequency strong ground motion. *Bulletin of the Seismological Society of America* 71 (6), 2071-2095.

Hartzell, S. H., and Heaton, T. H. (1983). Inversion of strong ground motion and teleseismic waveform data for the fault rupture history of the 1979 imperial valley, California, earthquake. *Bulletin of the Seismological Society of America* 78 (6), 1553-1583.

Havskov, J., and Ottemöller, L. (2010). *Routine data Processing in earthquake seismology*. Springker.

Hou, Z., Yang, Z., Qu, X., Meng, X., Li, Z., Beaudion, G., Rui, Z., Gao, Y., and Zaw, K. (2009). The Miocene Gangdese porphyry copper belt generated during post-collisional extension in the Tibetan Orogen. *Ore geology reviews* 36, 25-51.

Jin, G., Chen, Y. S., and Basang, C. R. (2009). Investigation of local earthquakes in the Lhasa region (in chinese). *Chinese Journal of Geophysics* 52 (12).

Kikuchi, M., and Kanamori, H. (1982). Inversion of complex body waves. *Bulletin of the Seismological Society of America* 72 (2), 591-506.

Kikuchi, M., and Kanamori, H. (1986). Inversion of complex body waves—Il. *Physics of the Earth and Planetary Inferiors* 43, 205-222.

Kikuchi, M., and Kanamori, H. (1991). Inversion of complex body waves--III. *Bulletin of the Seismological Society of America* 81 (6), 2335-2350.

Kikuchi, M., and Kanamori, H. (2003). Note on teleseismic body-wave inversion program. 1-21.

Langin, W. R., Brown, L. D., and Sandvol, E. A. (2003). Seismicity of central Tibet from project INDPTH III seismic recordings. *Bulletin of the Seismological Society of America* 93 (5), 2146-2159.

Lay, T., and Wallace, T. C. (1995). *Modern global seismology*. Academic press.

Li, D. W. (2004). Late cenozoic intraplate orogeny and dynamic metallogeny in the southern Qinghai-Tibet Plateau. *Earth science fronties* 11 (4).

Li, H. O., Xu, X. W., Jiang, M., and Ma, W. T. (2010). Crustal structure under Banggong-Nujiang suture and terrain assembly model of Lhasa and Qiangtang block in the western Qinghai-Tibet plateau. *Seismolgy and geology* 32 (2).

Mercier, J. L., Armijo, R., Tapponnier, P., Evelyne, C. G., and Lin, H. T. (1987). Change from late tertiary compression to quaternary extension in southern Tibet during the India-Asia collision. *Tectonics* 6, 275-304.

Molnar, P., and Tapponnier, P. (1978). Active of tectonics of Tibet. *J. Geophys. Res.* 83, NO. Bll, 5361-5375.

Molnar, P., England, P., and Martinod, J. (1993). Mantle dynamics, uplift of the Tibetan Plateau, and the Indian monsoon. *Reviews of Geophysic* 31, 357-396.

Motazedian, D., and Atkinson, G. M. (2005). Stochasitic finite-fault modeling based on a dynamic corner frequancy. *Bulletin of the Seismological Society of America* 95 (3), 995-1010.

Motazedian, D., and Moinfar, A. (2006). Hybrid stochastic finite fault modeling of 2003, M6.5, Bam earthquake (Iran). *journal of seismology* 10, 91-103.

Ni, J., and York, J. E. (1978). Late Cenozoic tectonics of the Tibetan Plateau. *J. of Geophys. Res.* 83(B11), 5377-5384.

Ni, J., and Barazang, M. (1984). Seismotectonics of the Himalayan collision zone: Geometry of the underthrusting Indian plate beneath the Himalaya. *J. of Geophys. Res.* 89 (B2), 144-1163.

Ou, G. B., and Herrmann, R. B. (1990). A statitical model for ground motion produced by earthquake at local and regional distances. *Bulletin of the Seismological Society of America* 80 (6).

Pan, Y. S. (1999). Formation and uplifting of the Qinghai-Tibet plateau (in chinese). *Earth science frontiers* 6 (3),

Qiao, X., You, X., Yang, S., Wang, Q., and Du, R. (2009). Study on dislocation inversion of Ms6.6 Damxung earthquake as constrained by InSAR measurement(in Chinese with English abstract). *Journal of geodesy and geodynamics* 29(6).

Qiao, X., Yang, S., Du, R., Ge, L., and Wang, Q. (2010). Coseismic slip from the 6 October 2008, Mw6.3 Damxung earthquake, Tibetan Plateau, constrained by InSAR observations. *Pure Appl. Geophys.*

Reese, C. C., Rapine, R. R., and Ni, J. F. (1999). Lateral variation of Pn and Lg attenuation at the CDSN station LSA. *Bulletin of the Seismological Society of America* 89 (1), 325-330.

Roumelioti, Z., and Beresnev, I. A. (2003). Stochastic finite-fault modeling of ground motions from the 1999 Chi-Chi, Taiwan, earthquake: Application to rock and soil sites

with implications for nonlinear site response. *Bulletin of the Seismological Society of America* 93 (4), 1691-1702.

Rthery, D. A., and Drury, S. A. (1984). The neoteconics of the Tibetan Plateau. *Tectonics* 3 (1), 19-26.

Shoja-Taheri, J., and Ghofrani. (2007). Stochastic finite-fault modeling of strong ground motions from the 26 December 2003 Bam, Iran, earthquake. *Bulletin of the Seismological Society of America* 97 (6), 1950-1959.

Shomali, Z. H., and Slunga, R. (2000). Body wave moment tensor inversion of local earthquakes: an application to the South Iceland Seismic Zone. *Geophys. J. Int.* 140, 63-70.

Stein, S., and Wysession, M. (2003). *An introduction to seismology,earthquakes, and earth structure*. Blackwell publishing.

Tapponnier, P., Mercier, J. L., Armijo, R., Tonglin, H., and Zhou, J. (1981). Field evidence for active normal faulting in Tibet. *Nature* 294.

Technology, T. C. o. S. a., and Archives, T. (1982). *Tibet earthquake compilations of historical material (in Chinese)*. Tibet People's Publishing House

Wu, Z. H., Ye, P. S., and Wu, Z. H. (2009). The seismic intensity,seismogenic tectonica and mechanism of the Ms6.6 Damxung earthquake on Oct 6,2008 in southern Tibet,China(in Chinese). *Geological bulletin of China* 28(6), 713-725.

Wu, Z. H., Ye, P. S., Barosh, P. J., and Wu, Z. H. (2010). The October 6, 2008 Mw 6.3 magnitude Damxung earthquake, Yadong-Gulu rift,Tibet, and implications for present-day crustal deformation within Tibet. *Journal of Asian Earth Sciences* 1-15.

Wu, Z. M., Shentu, B. M., Cao, Z. Q., and Deng, Q. D. (1990). The surface ruptures of Damxung (Tibet) earthquake (M=8) in 1411 (in chinese). *Seismology and geology* 12 (2).

Wu, Z. M., Cao, Z. Q., Shen-tu, B. M., and Deng, Q. D. (1992). Active fault in the central Tibet. *Seismological Press, Beijing* 161–192.

Xie, J. k. (2002). Lg Q in the Eastern Tibetan Plateau. *Bulletin of the Seismological Society of America* 92 (2).

Xing, L. L., Li, J. C., Zou, Z. B., and Zhou, X. (2007). Stsudy on seismo-tectonic dynamics of Qinghai-Tibet plateau from isostatic gravity anomalies (in chinese). *Journal of geodesy and geodynamics* 27 (6).

Yalcinkaya, E. (2005). Stochastic finite-fualt modeling of ground motions from the June 27,1998 Adana-Ceyhan earthquake. *Earth planets space* 57, 107-115.

Yuntai, C., Zhongliang, W., Peide, W., lisheng, X., Hongji, L., and Qirui, M. (2000). *Digital seismology (in Chinese)*. Earthquake publishing.

Zeng, R. S., Ding, Z. F., Wu, Q. J., and Wu, J. P. (2000). Seismological evidences for the multiple incomplete crustal subductions in Himalaya and southern Tibet. *Chinese Journal of Geophysics* 43 (6).

Zhang, P. Z., Shen, Z., Wang, M., Gan, W., Roland, B., Molar, P., Wang, Q., Niu, Z., Sun, J., Wu, J., Sun, H., and You, X. (2004). Continuous deformation of the Tibetan Plateau from global positioning system data. *Geology* 32(9), 809–812.

Zhang, X. M., Sun, R. M., and Teng, J. W. (2007). Studies of Qinghai-Tibet Plateau and its adjacent areas crust, lithosphere and asthenosphere thickness (in chinese). *Science bulletin* 52 (3).

Zhang, X. M., Sun, R. M., Yang, H., and Teng, J. W. (2008). Application of improved simulated annealing algorithm in the study of depth of interfaces in the crust and upper mantle (in chinese). *Progeress in geophsics* 23 (4), 1023-1029.

Zhang, Y. L., Li, B. Y., and Zheng, D. (2002). A discussion on the boundary and area of the Tibetan Plateau in China (in chinese). *Geological Research* 21 (1).

References

Zhao, W., Mechie, J., BROwn, L. D., Guo, J., Haines, S., Hearn, T., Klemperer, S. L., Ma, Y. S., Meissner, R., Nelson, K. D., Ni, J. F., Pananont, P., Rapine, R., Ross, A., and Sau, J. (2001). Crustal structure of central Tibet as derived from project INDEPTH wide-angle seismic data. *Geophys. J. Int.* 145, 486-498.

Appendix-Ⅰ

Matlab programs for stochastic finite-fault method

```
% Program 1: Acceleration time series
% Block 1 for simulated acceleration time series
clear
fidin=fopen('out_acc_s001.out');
fidout=fopen('accs001.txt','w');
    skipheadline=0;
while ~feof(fidin)
        skipheadline=skipheadline+1;
    tline=fgetl(fidin);
    if skipheadline>12
        fprintf(fidout,'%s\n',tline);
        continue
    end
end
fclose(fidout);
outdata=importdata('accs001.txt');
% Next 3 lines for making the same time scale
addend(1:295)=0;
simuacc=[outdata(296:1600,2);addend'];
time=0:0.05:79.95;
subplot(4,1,1)
plot(time,simuacc,'LineWidth',1.5)
text(45,-12,'EXSIM, this study');
set(gca,'XTick',[0 10 20 30 40 50 60 70]);
set(gca,'yTick',[-20 -10  10 20]);
axis([0 70 -20 20])
% Next 7 lines for maximum value of the simulation acceleration
PGAsimulation1=max(outdata(:,2))
PGAsimulation2=-min(outdata(:,2))
if PGAsimulation1>PGAsimulation2
        SIMPGA=PGAsimulation1;
  else
        SIMPGA=PGAsimulation2;
end
text(45, 12,['PGA=', num2str(SIMPGA)]);
% End the block 1
```

```matlab
% Block 2 for observed acceleration time series E-W
fidin=fopen('LSA00BHE.txt');
fidout=fopen('LSABHE.txt','w');
    skipheadline=0;
while ~feof(fidin)
        skipheadline=skipheadline+1;
    tline=fgetl(fidin);
    if skipheadline>30
        fprintf(fidout,'%s',tline);
        continue
    end
end
fclose(fidout);
accBHE=importdata('LSABHE.txt')*100; % 100 for changing unit
BHE=accBHE(6001:7600)';
timeBHE=0:0.05:79.95;
subplot(4,1,2)
plot(timeBHE,BHE,'LineWidth',1.5)
text(45,-12,'Observed E-W');
set(gca,'XTick',[0 10 20 30 40 50 60 70]);
set(gca,'yTick',[-20 -10 10 20]);
axis([0 70 -20 20]),ylabel('Acc (cm/s^2)')
% Next 7 lines for maximum value of the simulation acceleration
PGABHE1=max(BHE(:,1));
PGABHE2=-min(BHE(:,1));
  if PGABHE1>PGABHE2
      PGABHE=PGABHE1;
  else
      PGABHE=PGABHE2;
  end
  text(45, 12,['PGA=', num2str(PGABHE)]);
 % End the block 2

% Block 3 for observed acceleration time series N-S
fidin=fopen('LSA00BHN.txt');
fidout=fopen('LSABHN.txt','w');
    skipheadline=0;
while ~feof(fidin)
        skipheadline=skipheadline+1;
    tline=fgetl(fidin);
```

```
    if skipheadline>30
        fprintf(fidout,'%s',tline);
        continue
    end
end
fclose(fidout);
accBHN=importdata('LSABHN.txt')*100;
timeBHN=0:0.05:79.95;
BHN=accBHN(5868:7467)';
subplot(4,1,3)
plot(timeBHN,BHN,'LineWidth',1.5)
text(45,-12,'Observed N-S');
set(gca,'XTick',[0 10 20 30 40 50 60 70 ]);
set(gca,'yTick',[-20 -10 10 20]);
axis([0 70 -20 20])
% Next 7 lines for maximum value of the simulation acceleration
 PGABHN1=max(BHN(:,1));
 PGABHN2=-min(BHN(:,1));
  if PGABHN1>PGABHN2
      PGABHN=PGABHN1;
  else
      PGABHN=PGABHN2;
  end
  text(45, 12,['PGA=', num2str(PGABHN)]);
 % End the block 3


% Block 4 for observed acceleration time series vertical comp.
fidin=fopen('LSA00BHZ.txt');
fidout=fopen('LSABHZ.txt','w');
    skipheadline=0;
while ~feof(fidin)
       skipheadline=skipheadline+1;
    tline=fgetl(fidin);
    if skipheadline>30
        fprintf(fidout,'%s',tline);
        continue
    end
end
fclose(fidout);
accBHZ=importdata('LSABHZ.txt')*100;
```

```
timeBHZ=0:0.05:79.95;
BHZ=accBHZ(5981:7580)';
subplot(4,1,4)
plot(timeBHZ,BHZ,'LineWidth',1.5)
text(45,-12,'Observed Vertical');
set(gca,'XTick',[0 10 20 30 40 50 60 70]);
set(gca,'yTick',[-20 -10 10 20]);
axis([0 70 -20 20])
xlabel('Time (sec)')
% Next 7 lines for maximum value of the simulation acceleration
   PGABHZ1=max(BHZ(:,1));
 PGABHZ2=-min(BHZ(:,1));
  if PGABHZ1>PGABHZ2
      PGABHZ=PGABHZ1;
  else
      PGABHZ=PGABHZ2;
  end
  text(45, 12,['PGA=', num2str(PGABHZ)]);
 % End the block 4


 % Block 5 for acceleration response spectra
  NsimuE=[BHN,simuacc,BHE];
  threecompacc=[BHZ,BHN,BHE];
  save NsE.txt -ascii  NsimuE
  save ZNE.txt -ascii  threecompacc
% End the block 5


% Program 2: Acceleration response spectra
 clear all
% Block 1 for simulated acceleration response spectra
NsimuE=load('specaNsE');
 freq=NsimuE(:,1);
 simu=NsimuE(:,3);
loglog(freq,simu,'LineWidth',1.5)
set(gca,'XTick',[ 0.02 0.1 0.5 1 4 10 ]);
set(gca,'yTick',[ 1 5 20 50]);
axis([0.02 10 0.15 60])
hold on
```

```
% Block 2 for observed acceleration response spectra
psacc=load('specaZNE');
psaBHZ=psacc(:,2);
psaBHN=psacc(:,3);
psaBHE=psacc(:,4);
loglog(freq,psaBHZ,'c','LineWidth',1.5)
set(gca,'XTick',[ 0.02 0.1 0.5 1 4 10 ]);
set(gca,'yTick',[ 1 5 20 50]);
axis([0.02 10 0.15 60])
 hold on
loglog(freq,psaBHN,'r','LineWidth',1.5)
loglog(freq,psaBHE,'k','LineWidth',1.5)
legend('EXSIM this study','Observed vertical','Observed NS','Observed
EW')
xlabel('Frequency (Hz)'), ylabel('Acc response spectra (cm/s^2)')
```

Appendix-II

Input file for the EXSIM programs of chapter 5

!Control file for program exsim_beta
!Revision of program involving a change in the control file on this date:
  02/18/09
!Title
  Runs for comparing exsim_beta with EXSIM_dmb
!MW, Stress, flag (0=fmax; 1=kappa), fmax or kappa
 5.89 60.0 1   0.04
!lat and lon of upper edge of fault
 29.66 90.50
!strike,dip, depth of fault
 188.8 51.6 11.0
!fault length and width, subfault length and width
 15.00   14.00 1 1
!hypo location in (i,j)sub. i=0 or j=0 for a random hypo.
 1 1
!beta , rho, y (=vrup/beta),delta t
 3.6 2.85 0.8 0.002
!gsprd: rg1,rg2,pow1,pow2,pow3
 70 140 -1.0 +0.0 -0.5
!Q: Q0,eta, Qmin
   126.0 0.37 1000.0
!trilinear duration and properties (rmin,rd1,rd2,durmin,b1,b2,b3)
  10. 70. 130. 0.0 0.16 -0.03 0.04
!Type of window: 1 for Saragoni-Hart taper windows, 0 for tapered boxcar window
 1
!low-cut filter corner(0-> no filter), nslope
 0.0 8
! %damping of response spectra
 5.0
!# of f and Min and Max F for response spectra(Max F should be less than Nyquist F
from delta t)
  100 0.1   20.
!no. of frequencies for summary output (10 max):
 5
!frequencies in summary output (-1.0 for pgv and 99.0 for pga):
-1.0 99.0 0.1 0.2 5
!Output file names stem:
out

!Name of crustal amplification file:
  ab06_hr_crustal_amps.txt
!No. of frequencies in the crustal amplification file
  5
!Name of site amplification file:
  siteAmplification.txt
!No. of frequencies in the site amplification file (0 to skip)
  0
!Low frequencies taper(0=Boore's taper, 1=Motazedian's taper), low frequency Coef for Motazedian's taper(needs and entry)
  1   -.5
!Pulsing Percent
  50.0
!deterministic flag(use 0!),gama,nu,t0, impulse peak
  0   1.0 90.0 4.0 10.
!iseed, # of trials
  309 10
!Number of Sites, coord flag (1=lat,long; 2=R,Az; 3=N,E)
  1 1
!Coordinates of each site
  29.70   91.13
!islipweight=-1 -> unity slip for all subfaults,=0 -> specify slips below, =1 -> random weights
  -1
!Matrix of slip weights
 1.0 1.0 1.0 1.0 1.0
 1.1 1.3 1.4 1.1 1.0
 1.1 1.4 1.5 1.2 1.2
 1.2 1.5 1.6 2.2 1.3